

**The Landfall and Inland Penetration of a Flood-Producing Atmospheric River in Arizona.**  
**Part II: Sensitivity of modeled precipitation to terrain height and atmospheric river orientation**

MIMI HUGHES, KELLY M. MAHONEY,

*Cooperative Institute for Research in the Environmental Sciences and NOAA/ESRL, Boulder, CO*

PAUL J. NEIMAN,

*NOAA/Earth System Research Laboratory/Physical Sciences Division, Boulder, CO*

BENJAMIN J. MOORE,

*Department of Atmospheric and Environmental Sciences, University at Albany, State University of New York, Albany, NY*

MICHAEL ALEXANDER, F. MARTIN RALPH

*NOAA/Earth System Research Laboratory/Physical Sciences Division, Boulder, CO*

Corresponding author address:

Mimi Hughes

NOAA/Earth System Research Laboratory

Physical Sciences Division

Mail Code R/PSD2; 325 Broadway

Boulder, Colorado 80305

Email: Mimi.Hughes@noaa.gov

To be submitted to: *Journal of Hydrometeorology*  
Summer 2013

Keywords: atmospheric river, orographic precipitation, WRF, terrain resolution

## 1   **Abstract**

2           This manuscript documents numerical modeling experiments based on a Jan 2010  
3   atmospheric river (AR) event that caused extreme precipitation in Arizona. The control  
4   experiment (CNTL), using the Weather Research and Forecast (WRF) model with 3-km grid  
5   spacing, agrees well with observations. Sensitivity experiments in which (a) model grid spacing  
6   decreases sequentially from 81 km to 3 km, and (b) upstream terrain is elevated, assesses the  
7   sensitivity of interior precipitation amounts and horizontal water vapor fluxes to model grid  
8   resolution and height of Baja California's terrain. The drying ratio, a measure of airmass drying  
9   after passage across terrain, increases with Baja's terrain height and decreases with coarsened  
10   grid spacing. Subsequently, precipitation across Arizona decreases as Baja's terrain height  
11   increases, and increases with coarsened grid spacing. Northern Baja's drying ratio is much larger  
12   than that of southern Baja, and thus ARs with a southerly enough trajectory to pass south of the  
13   higher mountains of northern Baja and still move into Arizona can produce greater precipitation  
14   in Arizona.

15           Further experiments are performed using a linear model of orographic precipitation (LM)  
16   for a central-Arizona-focused subdomain. The actual incidence angle of the AR ( $211^\circ$ ) is close  
17   to the optimum angle for large region-mean precipitation. Changes in region-mean precipitation  
18   amounts are small due to AR angle changes, however changes in basin-mean precipitation  
19   amounts of 33% are seen within the range of physically plausible AR angles tested. Larger LM  
20   precipitation sensitivity is seen with the Baja-terrain-modification experiments than with AR-  
21   angle modification.

22

## 23 1. Introduction

24 Wintertime precipitation along the west coast of the United States often occurs as the  
25 result of large water vapor fluxes from atmospheric rivers (ARs) – long, narrow, low-level  
26 plumes of enhanced water vapor transport (Zhu and Newell 1998) – impinging on local  
27 topography. When AR-containing cyclones make landfall on the western U.S. coast, their  
28 enhanced vertically integrated water vapor transport (IVT; see Eq. 1 in section 2c) combines  
29 with near-neutral moist static stability (Ralph et al. 2005; Neiman et al. 2008b) and strong  
30 orographic forcing (e.g. Smith et al. 2010) to produce large amounts of precipitation (Neiman et  
31 al. 2008a, Dettinger 2004). Consequently, AR storms have been linked with flooding, and are a  
32 critical component of the water budget of the western U.S. (Ralph et al. 2006; Dettinger 2011;  
33 Dettinger et al. 2012).

34 Although much headway has been made documenting the importance of ARs to extreme  
35 precipitation on the west coast of the U.S., only a few studies have documented the impact of  
36 ARs across the U.S. intermountain west (Leung and Qian 2009; Rutz and Steenburgh 2012, Rutz  
37 et al. 2014; Rivera et al. 2014). Part I of this two-part series (Neiman et al. 2013, hereafter PT1)  
38 examined a sequence of three strong flood-producing AR events that occurred in late January  
39 2010 and produced large amounts of precipitation across the southwestern U.S. In many  
40 locations across the southwest U.S., this series of storms ranked in the top 5% of precipitation  
41 events since 1950, and it caused record precipitation and widespread flooding, especially across  
42 central Arizona’s Mogollon Rim, which stretches from northwest to southeast across central  
43 Arizona (see Fig. 1d). The strongest AR, and the last in the sequence, formed north of Hawaii on  
44 19 Jan. 2010. It moistened via water vapor convergence and strong latent heat fluxes within the

45 marine boundary layer, made landfall, and moved inland from 20-22 Jan. 2010. The strong IVT  
46 associated with this AR, combined with its moist neutral stratification that allowed strong  
47 ascending airflow as the AR crossed Arizona's complex topography (e.g. Rotunno and Ferretti  
48 2001), resulted in widespread precipitation, while the AR's high melting levels and soils  
49 saturated by the preceding AR events contributed to widespread flooding. The resultant  
50 orographic precipitation and hydrological impacts from the AR of 20-22 Jan. were comparable to  
51 those typically observed with landfalling ARs in the west-coast mountains. Because of the  
52 severity of this series of storms, including loss of life during impact, the meteorology and  
53 National Weather Service (NWS) response were the subject of a multi-office NWS local service  
54 assessment (personal communication, Paul Iñiguez, General Forecaster, WFO Phoenix,  
55 Arizona).

56 Inland-penetrating ARs encounter the mountainous terrain of the western U.S, which  
57 plays an important role in determining water vapor loss along the storm's path. PT1 postulated  
58 that for this specific event, the upstream topography was particularly critical in determining  
59 downstream precipitation amounts: "... the intense character of the incoming vapor fluxes was  
60 partly a consequence of the precise positioning of the AR across the relatively low mountains of  
61 southern Baja south of 30°N (rather than across the much higher, northern portion of this range)  
62 and west of Mexico's Sierra Madre Occidental, because only a fraction of the water vapor within  
63 the AR over the eastern Pacific was likely lost to orographic processes upwind of Arizona." We  
64 test this observationally-based hypothesis using two sensitivity experiments with the Weather,  
65 Research, and Forecast model (WRF). We first coarsen WRF's terrain, which impacts the height  
66 of the mountains, as well as the gradients associated with them; we focus on the reduction of  
67 Baja California terrain height due to reduced terrain grid spacing in this experiment. In the

68 second experiment we artificially increase Baja's terrain height to simulate AR passage across  
69 higher topographical barriers (e.g., Southern vs. Northern Baja). The goal of these experiments is  
70 to quantify how critical the passage of this AR across lower-altitude southern Baja was to  
71 precipitation amounts in Arizona by modifying WRF's terrain.

72 While the magnitude of water vapor fluxes incident on topography is a first-order  
73 determinant of resultant precipitation (e.g., Roe 2005; Smith 2006), the projection of those fluxes  
74 onto local terrain also determines precipitation magnitude. As the direction of the incoming  
75 water vapor fluxes is rotated, the magnitude of the dot product between the terrain gradient and  
76 those fluxes changes, modulating precipitation response (e.g., Smith 1979; Smith and Barstad  
77 2004). A few studies have suggested that AR angle is critical in determining local precipitation  
78 response because of its orientation relative to both upstream and local topography (Ralph et al.  
79 2003; Neiman et al. 2011). The third experiment in this manuscript quantifies the impact of AR  
80 angle on region-wide and basin-scale precipitation amounts, utilizing the one-layer linear model  
81 (LM) of orographic precipitation (Smith 2003; Smith and Barstad 2004) to artificially 'rotate' the  
82 AR that impacts Arizona's Mogollon Rim while keeping AR IVT magnitude fixed. We then use  
83 the LM on output from the terrain-modification WRF experiments so that AR-angle sensitivity  
84 can be directly compared with AR-IVT magnitude sensitivity.

## 85 **2. Model, data and methods**

### 86 *a. WRF simulations*

87 The sensitivity of precipitation to terrain height is tested using a set of nine simulations  
88 generated with the Weather Research and Forecasting model, version 3.3.1 (WRF; Skamarock et  
89 al 2008). To focus on the primary AR event from PT1, each simulation begins on 1800 UTC Jan

90 20, 2010 and runs for 48 hours, ending on 1800 UTC Jan. 22, 2010. Six of the nine simulations  
91 use the same 699x699 gridpoint atmospheric domain with 3-km grid spacing for the model  
92 atmosphere, and use identical physics parameterizations (CNTL, 9L3A, 27L3A, 81L3A, Tall,  
93 Taller; see Table 1 for short descriptions of each simulation). The physics parameterizations used  
94 for these six simulations are: Thompson microphysics (Thompson et al. 2008), explicit  
95 convection (i.e., no cumulus scheme is used<sup>1</sup>), rapid radiation transfer model longwave radiation  
96 (Iacono et al. 2008), Dudhia shortwave radiation (Dudhia 1989), Noah land surface model (Chen  
97 and Dudhia 2001), and the Yonsei University planetary boundary layer scheme (Hong et al.  
98 2006) with a Monin-Obukhov surface layer. The other three simulations cover the same  
99 geographical area as the previous six, but have atmospheric resolution commensurate with their  
100 coarsened terrain (9L9A, 27L27A, 81L81A), and thus have fewer gridpoints. These three  
101 simulations also use the Kain-Fritsch cumulus parameterization (Kain 2004) rather than explicit  
102 convection because of their coarsened atmosphere. All simulations have 54 vertical levels, and  
103 use the Climate Forecast System Reanalysis as lateral boundary conditions (see Section 2b).

104 Terrain from the WRF simulations is shown in Fig. 1. The control run (CNTL) is a  
105 standard WRF simulation using 3-km atmospheric grid spacing atop model terrain with 3-km  
106 grid spacing generated using the WRF preprocessing system (WPS); terrain of the three coarse-  
107 atmosphere simulations (9L9A, 27L27A, 81L81A) is generated similarly. We then used two  
108 different methods to modify terrain while keeping WRF grid spacing (i.e., atmospheric

Mimi Hughes 3/24/14 8:14 PM

**Comment [1]:** Text changed from here to the end of the paragraph to describe additional simulations.

---

<sup>1</sup> Sensitivity to having no cumulus scheme at 3 km grid spacing was tested by running an identical 3 km simulation with the Kain Fritsch cumulus parameterization. Resulting precipitation in this additional simulation was comparable to CNTL over land (not shown).

109 resolution) constant at 3 km. First, the terrain for the 3 coarse-resolution terrain, fine-resolution  
110 atmosphere simulations (81L3A, 27L3A, 9L3A) was generated using WPS, then the coarse-  
111 resolution terrain was interpolated using the nearest-neighbor technique to the 3-km grid used in  
112 CNTL. For the second method, two simulations were conducted in which the terrain in Baja  
113 peninsula was altered. In the “BajaTall” simulation, the existing terrain height was increased by a  
114 factor of 5 for lower (<300 m) elevations, and the height increase factor was decreased steadily  
115 for higher elevations, topping out with an increase factor of 1.1 for the highest elevations (over  
116 2500 m). Thus, the maximum terrain height was increased by less than 250 m, but the rest of the  
117 terrain was increased to be more commensurate with the higher elevation locations. These  
118 specific multiplication factors were chosen so that the maximum elevations across Baja didn’t  
119 increase much but ‘gaps’ in the terrain were eliminated and low-elevation South Baja was more  
120 comparable to North Baja. In the “BajaTaller” simulation the terrain was also altered, although  
121 using larger terrain height increase factors so that the maximum elevations across Baja were  
122 similar to maxima in the Mogollon region: lower (<300 m) elevations were increased by up to 7  
123 times their original value, and the height increase factor was again decreased steadily for higher  
124 elevations, topping out with an increase factor of 1.4 for elevations over 2500m. Figs. 1e and 1f  
125 illustrate the effect of these changes. We also smoothed terrain features at the northern edge of  
126 the altered terrain (where it meets the unaltered terrain of California) to eliminate unrealistically  
127 steep edges along the boundaries.

#### 128 *b. WRF verification datasets*

129 In section 3, IVT from CNTL is compared to that from the National Centers for  
130 Environmental Prediction (NCEP) Climate Forecast System Reanalysis (CFSR; Saha et al.

131 2010). For our calculations, we retrieved the analyses on a  $0.5^\circ \times 0.5^\circ$  grid and on pressure levels  
132 1000 hPa to 300 hPa, spaced every 25 hPa below 700 hPa and every 50 hPa above, on 0000 UTC  
133 Jan. 22, 2010.

134 Section 3 also compares precipitation and water-vapor transport variables from CNTL  
135 against observations used in PT1. The spatial distribution of 48-hour total precipitation in CNTL  
136 is compared to the 6-hourly accumulated NCEP Stage IV quantitative precipitation estimation  
137 (QPE) product (Lin and Mitchell 2005; Baldwin and Mitchell 1998), summed over the 48-h  
138 period starting at 1800 UTC 20 Jan and ending 1800 UTC 22 Jan 2010. Stage IV QPE is a  
139 nationally mosaicked, 4 km resolution gridded precipitation estimate created from the multi-  
140 sensor (i.e., radar- and gauge-based) precipitation estimates created at each river forecast center.

141 To assess the timing of WRF-generated precipitation, accumulated precipitation time series from  
142 three gauges in the Mogollon sub-region that were presented in PT1 (Workman Creek, Marshall  
143 Gulch, and Tucson) are compared to time series precipitation traces from CNTL at the nearest  
144 gridpoint. Along-AR bulk integrated water vapor (IWV) flux (see calculation method in Sect. 2c)  
145 at Tucson was calculated using IWV measurements calculated from a dual-channel global  
146 positioning system (GPS) receiver at Tucson combined with a NOAA 449-MHz radar wind  
147 profiler (White et al. 2007) deployed 48 km northwest of the Tucson GPS receiver.

#### 148 *c. Diagnostic calculations*

149 We calculate water vapor transport (VT) from wind ( $\vec{U}$ ) and specific humidity ( $q_v$ ) in both  
150 WRF simulations and CFSR. Prior to IVT calculation, WRF  $\vec{U}$  and  $q_v$  are interpolated from their  
151 native sigma coordinates to pressure levels every 25 hPa from 1000 hPa to 300 hPa. CFSR data  
152 is retrieved on pressure levels. From the pressure level data, we calculate layer-mean vapor

Mimi Hughes 3/29/14 6:39 PM

**Comment [2]:** Paul, I could not find clear documentation on this, but when I looked at the CBRFC webpage, clear radar outlines are visible on their MPE images. My guess is that all three (gauge, radar, and mountain mapper) are used; to keep this brief I'm going to leave the text as is unless you are unhappy with it.



153 transport every 50 hPa (similar to the IVT calculation in Neiman et al. 2008a):

$$\overline{VT} = \frac{1}{g} \int_{p_n}^{p_{n+1}} q_v * \vec{U} * dp$$

Eq. 1

154 where  $g$  is gravitational acceleration and  $p$  is pressure. This calculation results in layer-mean VT  
155 every 50 hPa from WRF data, which we then sum from 1000 to 300 hPa (which should include  
156 the majority of the tropospheric water vapor content) to compute IVT.

157 Because direct observations of IVT are not available, we estimate along-AR bulk IWV  
158 flux from observed IWV and wind profiles (as in PT1; see footnote on page 476), and then  
159 perform a similar calculation using WRF output at nearest gridpoints for comparison. Bulk IWV  
160 flux (Neiman et al. 2009) is defined as the product of IWV and winds in the ‘orographic  
161 controlling layer’ – the range of altitudes for which the upslope wind speeds correlate strongly  
162 with precipitation amounts. In this case we have used observed winds between 1.0 and 1.5 km  
163 above mean sea level (MSL), as in PT1. An AR orientation from 220° is assumed. The observed  
164 bulk IWV flux is then compared against CNTL bulk IWV flux calculated using a similar method.  
165 Specifically, the modeled bulk IWV flux is calculated using IWV at the gridpoint closest to the  
166 Tucson GPS receiver and model-averaged winds in the layer between 900 and 850 hPa (i.e., ~1.0  
167 – 1.5 km MSL) at the gridpoint closest to the 449-MHz wind profiler location.

168 To quantify the impact of Baja California’s topography on downstream moisture, we  
169 calculate the drying ratio (DR) for the nine WRF simulations in Section 4. DR is calculated using  
170 the formula from Kirshbaum and Smith (2008):

$$DR = 1 - \frac{IWT_{downstream}}{IWT_{upstream}} \quad \text{Eq. 2}$$

where IWT is total water transport, calculated exactly as IVT except using total atmospheric water content (i.e., the sum of water vapor, liquid, and ice) rather than water vapor content. The details of our calculation are discussed in Sect. 4.

#### *d. Linear model of orographic precipitation*

The AR-angle sensitivity experiments of Section 5 use the one-layer linear model of orographic precipitation developed in Smith (2003) and Smith and Barstad (2004), applied to the terrain of the CNTL simulation (i.e., 3 km grid spacing) and extended to account for upstream drying effects in Smith and Evans (2007). Here we describe this model briefly; more thorough descriptions and examples of its use can be found in Smith et al. (2005), Smith and Evans (2007), Hughes et al. (2009), and Lundquist et al. (2010). The LM describes the pattern of precipitation arising from forced ascent of saturated air over topography, where the vertical rate of ascent is determined from linear mountain wave theory. Forced ascent in the LM converts moist air to cloud water, which then converts to hydrometeors with timescale  $\tau_c$  and fall out with timescale  $\tau_f$ . The hydrometeors and cloud water are advected by a mean wind  $\vec{U} = U\mathbf{i} + V\mathbf{j}$ . The LM also includes a gravity wave term allowing the mountain-wave-induced change of vertical velocity with height to cause precipitation to fall upstream of topography gradients. Thus in the LM, precipitation broadly scales with the gradient of the terrain, modified by advection and gravity wave processes. For convenience the LM operates in Fourier space, where representations of physical processes can be combined into a single transfer function. A background precipitation rate, representing the precipitation falling at zero elevation far from

191 topographical influence, is then added to the inverse Fourier transform. The solution is then  
192 truncated to eliminate negative values.

193 Smith and Evans (2007) illustrate how the relationship between the water vapor flux far  
194 upstream, the drying ratio, and the local precipitation can be combined to incorporate the effects  
195 of airstream drying into the linear model. Prior to accounting for drying, the reference LM  
196 precipitation amount,  $P_{ref}$ , depends on the water vapor transport far upstream,  $\overrightarrow{IVT_0}$ . The local  
197 precipitation is then assumed to be this reference precipitation modified by the drying ratio (Eq.  
198 2):

$$P(x, y) = P_{ref}(x, y) \times (1 - DR(x, y))$$

Eq. 3

199 Then, the relationship between the drying ratio and reference precipitation is invoked, and the  
200 first-order differential equation that results is solved, to relate the local precipitation directly to  
201 the reference precipitation and water vapor transport far upstream:

$$P(x, y) = P_{ref}(x, y) \times \exp \left\{ - \int_{upstream}^{x, y} \frac{P_{ref}(x, y) ds}{|\overrightarrow{IVT_0}|} \right\}$$

Eq. 4

202 where the integral is calculated along the wind direction, and thus  $ds = (Udx + Vdy)/|\overrightarrow{U}|$ .

203 Although another extension of the LM incorporating multiple layers has recently been  
204 developed (Barstad and Schüller 2011), the simpler one-layer version is more appropriate to  
205 investigate the impact of modifying (via angle and terrain height) impinging IVT on the  
206 precipitation distribution, since IVT is a vertically integrated quantity.

207

Mimi Hughes 3/24/14 10:25 PM

**Comment [3]:** Added this entire paragraph to summarize modifications to original LM to incorporate drying effects.

### 3. Comparison of CNTL to observations

To assess WRF's ability to represent the meteorological processes critical to this event, and thus justify its use for the subsequent experiments, we first compare CNTL's precipitation with observations. Fig. 2a and 2b show the 48-hour (1800 UTC Jan. 20, 2010 to 1800 UTC Jan. 22, 2010) total precipitation from NCEP's Stage IV QPE product and CNTL, respectively, where locations with missing data in Stage IV have been masked out in CNTL. Visual comparison of these two figures illustrates that CNTL's precipitation is quite realistic: both indicate large amounts of precipitation across southern California's mountains and the Mogollon Rim in Arizona, with moderate amounts in southwest Colorado's San Juan mountains, and smaller amounts of precipitation across most of the southwestern US. The agreement between the two datasets is confirmed by a high spatial correlation (correlation coefficient = 0.83). Fig. 2c compares areal mean and maximum precipitation amounts for three of the four sub-regions of Fig. 1b: The areal mean precipitation in the Mogollon sub-region (i.e., blue box labeled 'Mogollon' in Fig. 1d) in WRF is 57.99 mm, ~ 5% greater than the stage IV mean precipitation of 55.4 mm, although the maximum precipitation in the Mogollon region is ~20% larger in WRF (315 mm vs. 263 mm). The spatial distribution of precipitation in the San Juan Mountains in southwest Colorado is similar in the model and observations, but CNTL precipitation is 30-40% larger. Comparable agreement is seen in the AZ/MX sub-region. Given Stage IV's known underrepresentation over complex terrain (e.g. Zhang et al. 2012), these comparisons suggest that CNTL is capturing precipitation quite well throughout the regions of interest. In addition, simulations performed at 1 km grid spacing (not shown) have mean precipitation amounts within 3% of CNTL in all four regions, suggesting higher resolution would not improve the agreement with observations.

231 To assess precipitation timing, we also compare CNTL precipitation with three gauges  
232 over a range of elevations in the Mogollon sub-domain that were first presented in PT1: Tucson  
233 (778 m MSL), Marshall Gulch (2171 m MSL), and Workman Creek (2103 m MSL) (Fig. 2d). At  
234 both Tucson and Workman Creek, the onset of precipitation is delayed in CNTL by a few hours,  
235 and overall precipitation is slightly underestimated in CNTL. At Marshall Gulch CNTL  
236 precipitation leads observations slightly and overestimates precipitation. Nevertheless, given that  
237 these are point estimates compared directly against CNTL's 3-km grid, the agreement is  
238 acceptable.

239 Since the precipitation over the Mogollon sub-domain during this event was largely  
240 determined by the magnitude of the incoming IVT (PT1), we also compare CNTL IVT on 0000  
241 UTC Jan. 22, 2010 with CFSR and a time series of along-AR bulk IWV flux (Fig. 3). Although  
242 CFSR is not an independent verification dataset (since it was used as lateral boundary  
243 conditions), it is the closest thing we have to observed gridded IVT, and was qualitatively  
244 compared against satellite IWV estimates in PT1. Both CFSR and CNTL have southwesterly  
245 IVT greater than  $1000 \text{ kg m}^{-1} \text{ s}^{-1}$  stretching across Baja California into Arizona. The largest  
246 difference between the two IVT maps is the fine-scale structure in IVT (e.g., sharp IVT gradients  
247 especially in the core IVT region) in CNTL that is absent from CFSR due to the latter's coarser  
248 horizontal resolution. The time series of IWV and bulk IWV flux (Fig. 3c) also show CNTL is  
249 successfully simulating this event, i.e. the magnitude and timing of strong IWV closely match  
250 the observed GPS measurements. In addition, CNTL closely matches the overall magnitude of  
251 observed along-AR bulk IWV flux and mirrors its observed increase on Jan. 21, 2010 with a  
252 sudden reduction on 0600 Jan. 22, 2010 during the passage of a cold front.

#### 4. Terrain modification experiments

The performance of CNTL compared with observations and reanalysis data confirm that WRF represents the dominant physical processes determining the distribution of precipitation during this event. In this section, we use WRF to test the sensitivity of precipitation to terrain elevation, both from the perspective of reduced terrain height due to coarse model resolution and by increasing the height of the upstream terrain in Baja California.

##### *a. Precipitation*

Figure 4 shows 48-hour total precipitation across the entire WRF domain for CNTL (Fig. 4g), the six terrain resolution sensitivity runs (81L81A, 27L27A, 9L9A, 81L3A, 27L3A, and 9L3A in Fig. 4a-f), and the two Baja California terrain-modification runs (Tall and Taller in Fig. 4h and 4i, respectively). All nine simulations exhibit two broad similarities. First, they all have extensive moderate precipitation (20-40 mm) throughout much of the domain even in the absence of orographic forcing. Second, in all simulations, topography drives larger precipitation amounts – ranging from 60 to 100 mm in some places but exceeding 200 mm in many locations including the Sierra Nevada, Baja California, northwestern Mexico/southern Arizona, the Mogollon Rim in Arizona, and the San Juan Mountains in southwestern Colorado. Some large differences between the simulations are also immediately apparent: As terrain resolution decreases (i.e., moving from 3 km terrain down to 81 km terrain) less precipitation falls over Baja California. The sharp lines of large precipitation amounts at the edges of the terrain grid boxes in the coarse land/fine atmosphere simulations (Figs. 4d-f), most evident in Fig. 4d, are a direct result of coarse resolution terrain sitting underneath finer-resolution atmosphere. Conversely, as the height of Baja California is increased in the Tall and Taller experiments, the

275 amount of precipitation falling over Baja increases, and precipitation amounts immediately  
276 downstream (i.e., over the AZ/MX and Mogollon sub-regions of Fig. 1d) decrease with increased  
277 height along the spine of Baja's mountains.

278 To further quantify the differences in precipitation among the nine experiments, Fig. 5  
279 shows the mean precipitation amounts (normalized by dividing by region-mean of CNTL) across  
280 the four sub-regions shown in Fig. 1d. As illustrated in Fig. 4, mean precipitation amounts are  
281 reduced over Baja as terrain resolution is decreased, with the exception of simulation 9L9A. This  
282 decrease in precipitation over Baja implies a consequent increase in downstream IVT. Although  
283 this implied increase in downstream IVT further implies that mean precipitation in AZ/MX and  
284 the Mogollon should get larger as the terrain resolution gets coarser, the changes in region-mean  
285 precipitation amounts are small and variable. Mean precipitation in AZ/MX is largest in the  
286 27L27A run than any other, and generally larger in the coarse atmosphere simulations than in  
287 those with coarse-terrain/fine- atmosphere. The opposite is true in the Mogollon region: mean  
288 precipitation increases steadily in the coarse-terrain/fine-atmosphere simulations, but remains  
289 nearly constant in the coarse-atmosphere simulations. Mean precipitation in the San Juans sub-  
290 region generally increases as terrain resolution gets finer, although like the Baja region 9L9A has  
291 the largest region-mean precipitation. We hypothesize that these inconsistent changes in region-  
292 mean precipitation are caused primarily by the fundamental difference between using a  
293 convective parameterization with a coarse atmosphere and explicit convection over the fine  
294 atmosphere, confounded by the differences in terrain in the three interior regions. Because of the  
295 lack of a clear signal, we further explore the drying across Baja in section 4b, and the sensitivity  
296 of downstream precipitation amounts in section 5.

Mimi Hughes 3/25/14 12:43 PM

**Comment [4]:** This entire paragraph was modified heavily.

297 Mean precipitation amounts in the Tall/er experiments show a physically plausible  
298 pattern across the four subregions: As Baja's terrain height increases mean precipitation amounts  
299 over Baja also increase. This increased precipitation over Baja results in a subsequent decrease  
300 over the remaining three regions, that gets smaller as the region's terrain gets higher (i.e., largest  
301 reduction in mean precipitation amounts over AZ/MX, followed by the Mogollon, and the  
302 smallest reduction over the San Juans). This pattern is more pronounced in Taller than in the Tall  
303 experiment (i.e., it scales with the changes in Baja's terrain height).

304 *b. IVT and drying ratio*

305 Because precipitation in this case is largely driven by orographic processes (e.g., see  
306 PT1), precipitation amounts should to first order be related to the product of integrated water  
307 vapor transport (IVT) and terrain gradient (e.g., Smith 2006). In this subsection, we investigate  
308 IVT in the different WRF experiments. Figure 6 shows IVT on 0000 UTC Jan. 22, 2010, when  
309 the AR was positioned directly across Baja and AZ. All simulations show IVT in excess of 1000  
310  $\text{kg s}^{-1} \text{m}^{-1}$  southwest of Baja, oriented from southwest to northeast across Baja and impinging on  
311 the Mogollon Rim in AZ, with broadly similar features. With the exception of 81L81A, these  
312 IVT values greater than  $1000 \text{ kg s}^{-1} \text{m}^{-1}$  extend southwestward from central Baja California in a  
313 sharp band to approximately  $26^\circ \text{N}$ ,  $120^\circ \text{W}$ , suggestive of strong convergence ahead of a surface  
314 cold front. Focusing first on the terrain resolution runs, we see a very slight increase in the area  
315 downstream of Baja with IVT over  $1100 \text{ kg m}^{-1} \text{s}^{-1}$  as terrain resolution decreases, likely due to  
316 decreased rainout over Baja resulting from the lowering of terrain height there. This increase is  
317 more apparent in the coarse-atmosphere simulations (Fig. 6a-c) than in the coarse-terrain/fine-  
318 atmosphere simulations (Fig. 6d-f). Likewise, the large precipitation amounts across Baja in the

Mimi Hughes 3/29/14 6:47 PM

**Comment [5]:** Paul, I've modified the text here to be more clear about what I'm trying to point out: 81L81A is the only simulation without IVT greater than  $1000 \text{ kg s}^{-1} \text{m}^{-1}$  in the SW corner of the domain.



319 Tall/er experiments illustrated in Figs. 4 and 5 are consistent with a dramatic reduction of IVT  
320 immediately downstream (i.e., northeast) of Baja.

321 To provide a vertical perspective on how the topography is modifying water vapor  
322 transport, we show two vertical cross-sections of along-AR water vapor transport (VT) at the  
323 same time as the maps of IVT, 0000 UTC Jan 22, 2010 (Figs. 7 and 8; projection lines A-B and  
324 C-D, respectively shown in Fig. 6g). Along the spine of Baja (Fig. 7, cross section A-B) just  
325 south of 31°N, all simulations show VT greater than  $120 \text{ kg m}^{-1} \text{ s}^{-1}$  that extends from the surface  
326 (which varies in altitude) to 3 km MSL in the **terrain resolution simulations** and CNTL, and  
327 extends to 3.5 km in Tall and 4 km MSL in Taller. The 9L9A, 9L3A, CNTL, Tall, and, in  
328 particular, Taller simulations also have strong water vapor transport (i.e., greater than  $60 \text{ kg m}^{-1}$   
329  $\text{s}^{-1}$ ) through the narrow gaps in the mountains between 28°N and 30°N **(these gaps do not exist in**  
330 **terrain coarser than 9 km grid spacing)**. Examination of the two variables that make up VT –  
331 wind and specific humidity (not shown) – reveals that water vapor is very small above about 3  
332 km MSL in all simulations, and the increase in VT between 3 and 4 km MSL in the Tall and  
333 Taller experiments compared with CTNL is caused by much stronger winds at those altitudes. As  
334 was visible in the IVT planviews of Fig. 6, the sharpness of the VT gradient north of the region  
335 of strongest transport is strongly related to atmospheric resolution (c.f., Fig. 7a versus Fig. 7d).  
336 Across Baja, 81L81A and 81L3A has substantially more total atmosphere between 0 and 3 km  
337 than CNTL, resulting in a slight increased depth over which the large VT values exist because of  
338 the reduced terrain height; this is due entirely to large specific humidity values at these lower  
339 elevations (not shown). Thus, as terrain height increases, more water vapor is removed by the  
340 terrain and VT decreases, except when winds are accelerated over the higher terrain.

Mimi Hughes 3/25/14 3:02 PM

**Comment [6]:** From here to end of paragraph is greatly modified.

341 Downstream of Baja California (Fig. 8), the impact on VT of Baja's terrain is even more  
342 apparent that it was along the spine of Baja: As terrain resolution decreases and thus Baja's  
343 terrain altitude is reduced, VT downstream increases (c.f. Fig. 8a, 8d and Fig. 8g). Likewise, as  
344 Baja's terrain altitude is increased, VT downstream decreases (c.f. Fig. 8g and Figs. 8h, 8i). This  
345 reduction in downstream VT is also evident in precipitation amount that fell across Baja (as  
346 discussed in Section 4a).

347 Finally, to quantify this effect for all hours of the simulation, we calculate  $DR$  (see Sect.  
348 2c, Eq. 2) across Northern and Southern Baja (green and blue boxes in Fig. 6g, respectively) as a  
349 summation of each hour of the simulation. Figure 9 shows average  $DR$  for Northern and  
350 Southern Baja for each WRF experiment. An examination of  $DR$  confirms the instantaneous  
351 values of IVT and VT: as terrain resolution decreases and results in lower terrain heights over  
352 Baja California, less water is removed from the AR as it crosses Baja (i.e.,  $DR$  for CNTL is  
353 greater than for the lower terrain-resolution experiments). In addition, we see that  $DR$  is much  
354 larger across Northern Baja than Southern Baja, partially confirming the hypothesis laid out in  
355 PT1, that the intense character of the vapor fluxes incident on the Mogollon was partly a  
356 consequence of the precise positioning of the AR across the relatively low mountains of  
357 Southern Baja, rather than across the much higher, northern portion of this range. The impact of  
358 coarsened terrain on  $DR$  is greater in Northern Baja than in Southern Baja, likely because the  
359 terrain of Southern Baja is already quite low and  $DR$ 's are already small in CNTL.

360 As the terrain height is increased in the Tall and Taller experiments,  $DR$  increases. Tall  
361 has only slightly raised terrain in Northern Baja, and Southern Baja was raised to be comparable  
362 in height to Northern Baja. The  $DR$  in this experiment increased by about 1/3, from 0.23 in

363 CNTL to 0.32 in BajaTall across Northern Baja, and has nearly doubled from 0.08 in CNTL to  
364 0.15 in BajaTall across Southern Baja. From a *DR* perspective, this experiment is the closest to  
365 answering the question of what would have happened if the AR never traversed Southern Baja  
366 but rather was more westerly in direction as it impinged on the Mogollon and crossed the higher,  
367 Northern Baja and Southern California terrain instead. Taller has much higher terrain along all of  
368 Baja California, and subsequently has much larger *DR*, that is, nearly double the CNTL across  
369 Northern Baja (CNTL *DR*=0.23, BajaTaller *DR*=0.42), and nearly triple CNTL across Southern  
370 Baja (CNTL *DR*=0.08, Baja Taller *DR*=0.22).

## 371 5. Sensitivity tests with the LM

372 Section 4 investigated the impact of terrain height on IVT across Baja and resultant  
373 precipitation and *DR* in the Mogollon and surrounding regions. In this section we examine the  
374 other dominant term in the upslope model of precipitation – the angle between the direction of  
375 the water vapor flux and the local terrain gradient – and test the sensitivity of resultant  
376 precipitation to that term by artificially ‘rotating’ the angle of the impinging AR. We focus solely  
377 on the Mogollon sub-domain (Fig. 10, with geographical context shown in Fig. 1d), and two  
378 river basins in the region, the Salt and the Verde (Fig. 10), the former of which was also  
379 discussed in PT1.

380 To ‘rotate’ the AR impinging on the Mogollon sub-region, we employ the LM, which we  
381 described briefly in Section 2d. We apply the LM to the Mogollon sub-region only (Fig. 10),  
382 using an area near the SW corner of the Mogollon sub-region (115°W to 113°W and 31°N to  
383 33°N) as ‘upstream’ conditions; the actual LM domain extent extends slightly south and west of  
384 the Mogollon sub-domain to fully capture the orographic forcing along the south and west edges

385 of the sub-domain, however the ‘upstream’ region is still extends SW of the LM domain. The  
386 LM solution (i.e., precipitation intensity) was calculated using meteorological variables in this  
387 ‘upstream’ region (layer-averaged temperature, winds, stability) from CNTL for each hour with  
388 near-surface air in the ‘upstream’ region that would be saturated at the Mogollon elevation, and  
389 then summed to obtain total LM precipitation. To calibrate the LM, it was first run for a range of  
390  $\tau_f$  and  $\tau_c$  (fallout time and condensation time) values and a limited set of different layer means  
391 (averaging from near-surface to anywhere between 900 and 700 hPa) for the meteorological  
392 variables. The 48-hour LM precipitation from these sensitivity runs was then compared against  
393 CNTL precipitation. Averaging from near-surface to 800 hPa,  $\tau_f=1250$  s, and  $\tau_c=900$  s were  
394 chosen by minimizing mean-Mogollon and max-Mogollon LM precipitation errors (compared  
395 against CNTL) in these sensitivity runs.

396 A comparison of the resultant LM precipitation, hereafter called LM CNTL (Fig. 11b)  
397 with that from CNTL (Fig. 11a) reveals that the LM has a similar precipitation distribution to  
398 CNTL in this region when applied using meteorological conditions directly ‘upstream’. The  
399 magnitude and location of LM CNTL local precipitation maxima is close to CNTL across many  
400 of the terrain features. However, LM CNTL overestimates the amount of precipitation that falls  
401 across many of the terrain features, particularly in the eastern portion of the sub-domain. The LM  
402 CNTL precipitation is also a bit too localized, and leeside precipitation amounts are too small.  
403 For these reasons, we will only compare LM results with other LM results, and not directly with  
404 the WRF precipitation amounts shown in Section 4.

405 To adjust AR ‘angle’ (i.e., the angle maximum IVT hits topography), we then rotate the  
406 LM input winds by angle increments of 10 degrees ranging from -40 (more southerly) to +40

Mimi Hughes 3/25/14 4:26 PM

**Comment [7]:** Much of this paragraph has changed.

degrees (more westerly) from the CNTL direction, while keeping the other input parameters fixed. The heavy black arrow in Fig. 11b shows that the average wind direction during precipitating hours from CNTL is from the south-southwest (from  $211^\circ$ ), consistent with the snapshot of the AR shown in Fig. 6g. Fig. 12 shows the difference of the resultant LM precipitation from LM CNTL precipitation with winds rotated (a)  $-40^\circ$ , (b)  $-20^\circ$ , (c)  $+20^\circ$ , and (d)  $+40^\circ$  away from this control direction (with black arrows showing mean rotated wind direction). As the wind direction shifts, the amount and magnitude of precipitation falling across the terrain shifts accordingly. The largest precipitation changes occur across terrain that shifts from being primarily windward to in the rain shadow of other terrain as the LM input winds are rotated. Also, the region-maximum actually shifts from one mountain to another (i.e. region maxima at  $34.25^\circ\text{N}$ ,  $112.5^\circ\text{W}$  and  $33.5^\circ\text{N}$ ,  $108.5^\circ\text{W}$  when AR angle is shifted counterclockwise from CNTL; region maxima at  $32.5^\circ\text{N}$ ,  $110.75^\circ\text{W}$  and  $35^\circ\text{N}$ ,  $113.75^\circ\text{W}$  when AR angle is shifted clockwise from CNTL, not shown) causing dramatic local changes.

To directly compare the sensitivity of Mogollon precipitation to AR angle with its sensitivity to upstream terrain, we next find the LM solution for 3-km terrain using meteorological conditions from the 8 terrain-sensitivity simulations (not shown). In this case, the angle of the water vapor flux changes very little from one case to another (e.g., Fig. 6), but instead the magnitude of incoming water vapor flux changes – greater IVT reaches the Mogollon for smaller Baja California DRs (Fig. 9). Because the AR angle is not changing, the distribution of LM precipitation in these solutions changes little, but the magnitude varies dramatically.

We then repeat the Mogollon-region-wide mean calculations of Section 4 with these LM precipitation amounts (Fig. 13). Focusing on the impact of AR angle (Fig. 13a), we see that the

Mimi Hughes 3/26/14 11:31 AM

Comment [8]: Paragraph is heavily modified

429 region-mean normalized precipitation is a minimum when the average AR angle is 171° (rotated  
430 -40° from CTNL), then increases slightly as the AR angle is rotated just 10° clockwise, reaching  
431 its maximum when the AR is approximately 191° (rotated -20° from CNTL). The change in  
432 mean precipitation for every 10° shift is fairly small, and the largest mean value (61.6 mm when  
433 AR rotation is -20°) is only 6% larger than the smallest (57.9 mm when AR rotation is -40°). The  
434 impact of upstream terrain resolution on Mogollon-sub-region wide LM precipitation (Fig. 13b)  
435 has patterns that are, for the most part, consistent with the drying ratios of Figure 9: Region-  
436 mean LM precipitation amounts increase compared to LM CNTL as Baja's terrain height is  
437 reduced (i.e., terrain-resolution experiments) and decrease as it gets higher (i.e., in the  
438 BajaTaller experiments), although 9L9A and 27L27A show larger and 81L81A shows smaller  
439 Mogollon region-mean LM precipitation than expected from their drying ratio differences. The  
440 largest increases from LM CNTL are seen in the 81 km grid spacing simulations: the 81L81A  
441 LM solution has region-mean precipitation 9% larger than CNTL, while 81L3A LM solution has  
442 region-mean precipitation 14% larger than CNTL. This has important implications for coarse-  
443 resolution numerical weather and climate models (and downscalings of those models). A  
444 summary of these percentage-wise changes in LM precipitation amounts for the full set of  
445 simulations is shown in Table 1.

446 Why are the LM terrain resolution sensitivity precipitation amounts more consistent with  
447 the drying ratio changes with terrain grid spacing than the WRF precipitation amounts in the  
448 Mogollon region (Fig. 5b)? The most obvious reason for this is that the reduced terrain grid-  
449 spacing simulations (e.g., 81L81A) have lower elevation terrain over the Mogollon region: Even  
450 if larger IVT is impinging on the region, the coarsened terrain and consequent reduced terrain  
451 elevations and gradients may offset the impact this increased IVT has on region mean

Mimi Hughes 3/28/14 5:29 PM

**Comment [9]:** Paragraph added. I think this warrants discussion so I'd rather not cut it altogether, but I'm not sure where to put it. I tried it in the summary/discussion section and really didn't like it there at all.

452 precipitation. Thus the comparable Mogollon region-mean precipitation amounts seen across the  
453 WRF terrain grid spacing experiments may be the result of a cancellation of errors. The LM  
454 results, on the other hand, all have the same 3 km grid spacing terrain driving their precipitation  
455 response. This large LM sensitivity, consistent with the drying ratio sensitivity, supports the  
456 notion that there may be cancellation of errors leading to the precipitation amounts in Fig. 5b.

457 If we repeat this analysis for smaller, more hydrologically-relevant areas within the  
458 Mogollon sub-region – in particular two river basins that were heavily impacted during this  
459 event, the Salt River and the Verde River – we see some similarities with some notable  
460 differences (Fig. 14). Both river basins have somewhat reduced basin-mean precipitation  
461 sensitivity to changes in upstream terrain height, particularly to terrain height reductions due to  
462 increased grid spacing (Table 1). In terms of basin-mean sensitivity to AR ‘angle’, the Salt River  
463 basin is considerably more sensitive than the entire Mogollon sub-region (33% change from -20°  
464 to +40°; Table 1), and the Verde River basin is also more sensitive (33% change from -10° to  
465 +40°; Table 1). Thus while the region-wide mean precipitation showed rather small sensitivity to  
466 AR ‘angle’, the more localized and more hydrologically-relevant basin-wide means are very  
467 sensitive to the angle of the incoming water vapor flux.

468 Because we have used the LM for all of the experiments in this section, we can now  
469 directly compare the sensitivity of local precipitation to these two factors: the AR ‘angle’  
470 rotation and the upstream terrain height. While there is some variation depending on sub-region  
471 examined (i.e., Verde vs. Salt vs. entire Mogollon), LM precipitation sensitivity to upstream  
472 terrain is generally larger than sensitivity to AR ‘angle’. This makes intuitive sense: Strength of  
473 the water vapor flux acts as the upper/lower limit of the total amount of precipitation that can

Mimi Hughes 3/28/14 5:01 PM

**Comment [10]:** Paragraph is revised throughout to reflect new results.

Mimi Hughes 3/28/14 5:11 PM

**Comment [11]:** Paragraph modified somewhat.

474 fall, whereas AR ‘angle’ determines what percentage of that limit is forced out by lift over the  
475 topography. Nevertheless, physically plausible rotations of AR ‘angle’ caused changes in basin-  
476 mean precipitation as large as 33%, which could still have substantial hydrologic impacts.  
477 Furthermore, we acknowledge that the sensitivity to upstream terrain height was largely  
478 determined by our subjective choice in terrain modification, whereas the AR ‘angle’ rotations  
479 chosen are supported by the climatology of atmospheric rivers making landfall in the SW US  
480 (e.g., Neiman et al. 2008a; Rivera et al. 2014). In reality, AR ‘angle’ and upstream topography  
481 likely interact to determine individual basin susceptibility to ARs with different orientation  
482 impacting the interior of the western United States (as in Neiman et al. 2011).

## 483 6. Summary and Discussion

484 To begin addressing the role of upstream topography in determining water vapor influx to  
485 the intermountain west, this manuscript presents the second part of a two-part case study of an  
486 AR event that caused extreme precipitation in Arizona in Jan 2010. To assess the sensitivity of  
487 interior precipitation amounts and water vapor flux to model grid resolution and height of Baja  
488 California’s terrain, we perform a set of sensitivity experiments with the WRF model, using a 3-  
489 km WRF simulation as the CNTL. Sensitivity experiments were performed with WRF: (a) three  
490 simulations where model grid spacing decreases sequentially from 81 km to 27 km to 9 km, (b)  
491 three simulations where model terrain grid spacing decreases sequentially from 81 km to 27 km  
492 to 9 km while the atmospheric resolution remains fixed at 3 km, and (c) two simulations where  
493 upstream (i.e., Baja California) terrain is increased. CNTL IVT is compared to IVT from the  
494 CFSR, and WRF bulk IWV flux compared to bulk IWV flux calculated from GPS met and wind  
495 profilers. In addition, CNTL precipitation is compared against Stage IV QPE and gauges. These



496 model variables agree acceptably with observations, justifying our use of the CNTL simulation  
497 as a baseline for further sensitivity experiments.

498 The WRF experiments show as the terrain of Baja California is raised, larger amounts of  
499 precipitation fall across Baja, and smaller amounts fall across Arizona downstream of Baja; as  
500 terrain grid spacing is reduced, less precipitation falls across Baja, but precipitation amounts  
501 across Arizona change only minimally. This precipitation relationship is then investigated from a  
502 water vapor transport (VT) perspective: As terrain height in Baja increases, the terrain removes  
503 more water vapor and VT generally decreases downstream of Baja. Interestingly, the simulations  
504 with increased Baja terrain exhibit somewhat elevated VT maxima due to accelerated winds over  
505 their higher terrain. The VT relationship is then quantified by calculating the drying ratio of Baja  
506 California for the WRF simulations. The drying ratio across Baja increases when its terrain  
507 height is increased, and decreases as terrain grid spacing coarsens (i.e., as the Baja terrain  
508 becomes lower). Supporting a hypothesis presented in PT1, the drying ratio of northern Baja is  
509 much larger than that of southern Baja.

510 A linear model (LM) for orographic precipitation is used to address the importance of *i)*  
511 the angle of the AR relative to the topography it impinges on and *ii)* the upstream topography to  
512 precipitation in the Mogollon region. The actual incidence angle of the AR ( $211^\circ$ ) is close to the  
513 optimum angle for large region-mean precipitation. Changes in region-mean precipitation  
514 amounts of 6% are seen within the range of physically-plausible AR angles tested (i.e., from  $-40^\circ$   
515 to  $+40^\circ$  of that observed). However, changes in basin-mean precipitation amounts for the same  
516 range of AR angles are much larger (up to 33%), driving home the importance of representing  
517 orographic precipitation distribution at high resolution to resolve basin scales. To quantitatively

518 compare this sensitivity with precipitation sensitivity to Baja's terrain height, the LM is then  
519 applied using meteorological parameters (i.e., LM input data) from the terrain-sensitivity WRF  
520 simulations and CNTL Arizona terrain. Larger precipitation sensitivity is seen with the terrain-  
521 modification experiments (due to modification of incoming IVT magnitudes) than with AR angle  
522 modification (Table 1), although this depends strongly on the rather subjective modifications  
523 made to upstream terrain.

524 In reality, both upstream terrain (determined by an AR's trajectory) and AR angle interact  
525 to determine resultant precipitation. The specific situation for the Mogollon sub-region and  
526 Verde river basin is laid out schematically in Fig. 15. The impact of ARs making landfall in AZ  
527 that are more westerly than CNTL are limited by passage across the high terrain of Northern  
528 Baja, because of its larger *DR* than Southern Baja. The local orographic precipitation response to  
529 the AR angle incident on the topography in both the Verde and Salt river basins is largest for  
530 angles ranging from  $\sim 181^\circ$  to  $\sim 211^\circ$  (Fig. 14), with the angle of greatest response dependent on  
531 the basin itself. The AR of Jan. 20-22, 2010 caused widespread large precipitation amounts in the  
532 Mogollon sub-region because it fell within the range of angles where AR trajectory and local  
533 terrain effects both favor a large precipitation response, although had it been somewhat more  
534 southerly, the local precipitation in the Salt river basin would have likely been even more  
535 extreme.

536 While upstream-terrain modification is largely an artificial experiment, it allows for a  
537 clear hypothesis test, leading to better understanding of the sensitivity of inland-penetrating ARs  
538 and resulting precipitation to terrain grid spacing. This test has highly practical implications for  
539 global climate models, global operational forecast models, and reanalysis datasets that are

Mimi Hughes 3/30/14 7:43 PM

**Comment [12]:** Entire paragraph modified to reflect slightly modified schematic (and new results).

540 regularly run at grid spacing much coarser than 10 km. In particular, the 81L81A simulation  
541 (which is comparable resolution to current reanalysis and climate models) has far too much water  
542 vapor reaching AZ, evidenced by the drying ratio across the coarse terrain grid spacing (and  
543 therefore too-low) Baja California being approximately 30% too small. While the precipitation  
544 response to this is moderated by coarsened Arizona terrain in the 81L81A experiment, the LM  
545 solution shows large precipitation amounts for the 81L81A simulation. Subsequently, while  
546 downscaling coarse-resolution atmospheric data (e.g., reanalysis datasets or global climate  
547 models) can address the representation of fine-scale local processes, it doesn't account for  
548 processes outside the domain, in this case the impact of upstream topography on moisture  
549 transport. Downscaled simulations based on coarse resolution products could be very sensitive to  
550 the incoming IVT amounts (e.g., Hahn and Mass 2009), and large overestimates of IVT  
551 penetrating the intermountain west in coarse-resolution numerical products (e.g., McAfee et al.  
552 2011) could be a source of error in simulations and reanalysis that employ coarse resolution  
553 models.

554 *Acknowledgments.* This research is supported by the U.S. Bureau of Reclamation. Thanks to  
555 Chengmin Hsu for the mapping of the Salt and Verde River Basins. We also thank three  
556 anonymous reviewers whose comments greatly improved the manuscript.

557

558 **References**

- 559 Baldwin, M. E., and K.E. Mitchell, 1998: Progress on the NCEP hourly multi-sensor U.S.  
 560 precipitation analysis for operations and GCIP research. *2nd Symposium on Integrated*  
 561 *Observing Systems, 78th AMS Annual Meeting*, 10-11.
- 562 Barstad, I., and F. Schueller, 2011: An Extension of Smith's Linear Theory of Orographic  
 563 Precipitation: Introduction of Vertical Layers. *Journal of the Atmospheric Sciences*, **68**, 2695-  
 564 2709.
- 565 Chen, F., and J. Dudhia, 2001: Coupling an advanced land surface-hydrology model with the  
 566 Penn State-NCAR MM5 modeling system. Part I: Model implementation and sensitivity.  
 567 *Monthly Weather Review*, **129**, 569-585.
- 568 Dettinger, M., 2011: Climate Change, Atmospheric Rivers, and Floods in California - A  
 569 Multimodel Analysis of Storm Frequency and Magnitude Changes. *Journal of the American*  
 570 *Water Resources Association*, **47**, 514-523.
- 571 Dettinger, M., K. Redmond, and D. Cayan, 2004: Winter orographic precipitation ratios in the  
 572 Sierra Nevada - Large-scale atmospheric circulations and hydrologic consequences. *Journal of*  
 573 *Hydrometeorology*, **5**, 1102-1116.
- 574 Dettinger, M. D., and Coauthors, 2012: Design and quantification of an extreme winter storm  
 575 scenario for emergency preparedness and planning exercises in California. *Natural Hazards*, **60**,  
 576 1085-1111.
- 577 Dudhia, J., 1989: NUMERICAL STUDY OF CONVECTION OBSERVED DURING THE  
 578 WINTER MONSOON EXPERIMENT USING A MESOSCALE TWO-DIMENSIONAL  
 579 MODEL. *Journal of the Atmospheric Sciences*, **46**, 3077-3107.
- 580 Hahn, R. S., and C. F. Mass, 2009: The Impact of Positive-Definite Moisture Advection and  
 581 Low-Level Moisture Flux Bias over Orography. *Monthly Weather Review*, **137**, 3055-3071.
- 582 Hong, S.-Y., Y. Noh, and J. Dudhia, 2006: A new vertical diffusion package with an explicit  
 583 treatment of entrainment processes. *Monthly Weather Review*, **134**, 2318-2341.
- 584 HUGHES, M., A. HALL, and R. FOVELL, 2009: Blocking in Areas of Complex Topography,  
 585 and Its Influence on Rainfall Distribution. *JOURNAL OF THE ATMOSPHERIC SCIENCES*, **66**,  
 586 508-518.
- 587 Iacono, M. J., J. S. Delamere, E. J. Mlawer, M. W. Shephard, S. A. Clough, and W. D. Collins,  
 588 2008: Radiative forcing by long-lived greenhouse gases: Calculations with the AER radiative  
 589 transfer models. *Journal of Geophysical Research-Atmospheres*, **113**.

590 Kain, John S., 2004: The Kain–Fritsch convective parameterization: An update. *J. Appl. Meteor.*,  
591 **43**, 170–181.

592 Kirshbaum, D. J., and R. B. Smith, 2008: Temperature and moist-stability effects on midlatitude  
593 orographic precipitation. *Quarterly Journal of the Royal Meteorological Society*, **134**, 1183–  
594 1199.

595 Leung, L. R., and Y. Qian, 2009: Atmospheric rivers induced heavy precipitation and flooding in  
596 the western US simulated by the WRF regional climate model. *Geophysical Research Letters*,  
597 **36**.

598 Lin, Y. a. K. E. M., 2005: The NCEP Stage II/IV hourly precipitation analyses: development and  
599 applications. *19th Conf. on Hydrology, American Meteorological Society*.

600 Lundquist, J. D., J. R. Minder, P. J. Neiman, and E. Sukovich, 2010: Relationships between  
601 Barrier Jet Heights, Orographic Precipitation Gradients, and Streamflow in the Northern Sierra  
602 Nevada. *Journal of Hydrometeorology*, **11**, 1141–1156.

603 McAfee, S. A., J. L. Russell and P. J. Goodman, 2011: Evaluating IPCC AR4 cool-season  
604 precipitation simulations and projections for impacts assessment over North America. *Climate*  
605 *Dynamics*. **37**:2271–2287. DOI 10.1007/s00382-011-1136-8

606 Neiman, P. J., F. M. Ralph, G. A. Wick, J. D. Lundquist, and M. D. Dettinger, 2008a:  
607 Meteorological characteristics and overland precipitation impacts of atmospheric rivers affecting  
608 the West Coast of North America based on eight years of SSM/I satellite observations. *Journal*  
609 *of Hydrometeorology*, **9**, 22–47.

610 Neiman, P. J., A. B. White, F. M. Ralph, D. J. Gottas, and S. I. Gutman, 2009: A water vapour  
611 flux tool for precipitation forecasting. *Proceedings of the Institution of Civil Engineers-Water*  
612 *Management*, **162**, 83–94.

613 Neiman, P. J., L. J. Schick, F. M. Ralph, M. Hughes, and G. A. Wick, 2011: Flooding in Western  
614 Washington: The Connection to Atmospheric Rivers. *Journal of Hydrometeorology*, **12**, 1337–  
615 1358.

616 Neiman, P. J., F. M. Ralph, B. J. Moore, M. Hughes, K. M. Mahoney, J. M. Cordeira, and M. D.  
617 Dettinger, 2013: The Landfall and Inland Penetration of a Flood-Producing Atmospheric River  
618 in Arizona. Part I: Observed Synoptic-Scale, Orographic, and Hydrometeorological  
619 Characteristics. *Journal of Hydrometeorology*, **14**, 460–484.

620 Neiman, P. J., and Coauthors, 2008b: Diagnosis of an Intense Atmospheric River Impacting the  
621 Pacific Northwest: Storm Summary and Offshore Vertical Structure Observed with COSMIC  
622 Satellite Retrievals. *Monthly Weather Review*, **136**, 4398–4420.

623 Ralph, F. M., P. J. Neiman, and R. Rotunno, 2005: Dropsonde observations in low-level jets over  
624 the northeastern Pacific Ocean from CALJET-1998 and PACJET-2001: Mean vertical-profile  
625 and atmospheric-river characteristics. *Monthly Weather Review*, **133**, 889-910.

626 Ralph, F. M., P. J. Neiman, G. A. Wick, S. I. Gutman, M. D. Dettinger, D. R. Cayan, and A. B.  
627 White, 2006: Flooding on California's Russian River: Role of atmospheric rivers. *Geophysical*  
628 *Research Letters*, **33**.

629 Ralph, F. M., and Coauthors, 2003: The impact of a prominent rain shadow on flooding in  
630 California's Santa Cruz Mountains: A CALJET case study and sensitivity to the ENSO cycle.  
631 *Journal of Hydrometeorology*, **4**, 1243-1264.

632 Rivera, E., F. Dominguez and C. Castro, 2014: Atmospheric Rivers and Extreme Cool Season  
633 Precipitation Events in the Verde River Basin of Arizona. *J. Hydromet.* Early Online Release.  
634 doi: 10.1175/JHM-D-12-0189.1

635 Roe, G. H., 2005: Orographic precipitation. *Annual Review of Earth and Planetary Sciences*, **33**,  
636 645-671.

637 Rotunno, R., & Ferretti, R. (2001). Mechanisms of intense Alpine rainfall. *Journal of the*  
638 *Atmospheric Sciences*, 58(13), 1732-1749.

639 Rutz, J. J., and W. J. Steenburgh, 2012: Quantifying the role of atmospheric rivers in the interior  
640 western United States. *Atmospheric Science Letters*, **13**, 257-261.

641 Rutz, Jonathan J., W. James Steenburgh, F. Martin Ralph, 2014: Climatological Characteristics  
642 of Atmospheric Rivers and Their Inland Penetration over the Western United States. *Mon. Wea.*  
643 *Rev.*, **142**, 905–921. doi: <http://dx.doi.org/10.1175/MWR-D-13-00168.1>

644 Saha, S., and Coauthors, 2010: THE NCEP CLIMATE FORECAST SYSTEM REANALYSIS.  
645 *Bulletin of the American Meteorological Society*, **91**, 1015-1057.

646 Skamarock, W. C., J. B. Klemp, J. Dudhia, D. O. Gill, D. M. Barker, M. Duda, X.-Y. Huang, W.  
647 Wang and J. G. Powers, NCAR Technical Note, 2008.

648 Smith, RB; Evans, JP, 2007: Orographic precipitation and water vapor fractionation over the  
649 southern Andes. *J. Hydrometeorol.*, **8**, 3-19.

650 Smith, B. L., S. E. Yuter, P. J. Neiman, and D. E. Kingsmill, 2010: Water Vapor Fluxes and  
651 Orographic Precipitation over Northern California Associated with a Landfalling Atmospheric  
652 River. *Monthly Weather Review*, **138**, 74-100.

653 Smith, R., 1979: *The influence of mountains on the atmosphere*. B. Saltzman,  
654 Ed., *Adv. Geophys.*, **21**, 87-230.

655 Smith, R. B., 2003: A linear upslope-time-delay model for orographic precipitation. *Journal of*  
656 *Hydrology*, **282**, 2-9.

657 —, 2006: Progress on the theory of orographic precipitation. . *Special Paper 398: Tectonics,*  
658 *Climate, And Landscape Evolution*, Geological Society of America.

659 Smith, R. B., and I. Barstad, 2004: A linear theory of orographic precipitation. *Journal of the*  
660 *Atmospheric Sciences*, **61**, 1377-1391.

661 Smith, R. B., I. Barstad, and L. Bonneau, 2005: Orographic precipitation and Oregon's climate  
662 transition. *Journal of the Atmospheric Sciences*, **62**, 177-191.

663 Thompson, G., P. R. Field, R. M. Rasmussen, and W. D. Hall, 2008: Explicit Forecasts of Winter  
664 Precipitation Using an Improved Bulk Microphysics Scheme. Part II: Implementation of a New  
665 Snow Parameterization. *Monthly Weather Review*, **136**, 5095-5115.

666 Zhang, J., Qi, Y., Kingsmill, D., & Howard, K. (2012). Radar-based quantitative precipitation  
667 estimation for the cool season in complex terrain: case studies from the NOAA  
668 hydrometeorology Testbed. *Journal of Hydrometeorology*, *13*(6), 1836-1854.

669 Zhu, Y., and R. E. Newell, 1998: A proposed algorithm for moisture fluxes from atmospheric  
670 rivers. *Monthly Weather Review*, **126**, 725-735.

671

672 **Table 1:** List of WRF simulations and their abbreviations in the text.

Simulation abbreviation	Terrain resolution	Atmospheric resolution	Other notes
CNTL	3 km	3 km	
9L9A	9 km	9 km	Uses Kain Fritsch convective parameterization
9L3A	9 km	3 km	
27L27A	27 km	27 km	Uses Kain Fritsch convective parameterization
27L3A	27 km	3 km	
81L81A	81 km	81 km	Uses Kain Fritsch convective parameterization
81L3A	81 km	3 km	
Tall	3 km	3 km	Terrain across Baja raised so that gaps through terrain are ‘filled in’, and maximum elevation is similar to Baja max in CNTL.
Taller	3 km	3 km	Terrain across Baja raised so that gaps through terrain are ‘filled in’, and maximum elevation is similar to Mogollon region max in CNTL.

673  
674  
675  
676  
677  
678  
679  
680  
681  
682  
683  
684  
685



686 **Table 2:** Percent change in mean precipitation amounts for the various LM solutions. Values  
687 have been calculated as follows: Total percent difference = (max-min)/min; max increase  
688 from CNTL = (max-CNTLp)/CNTLp; max decrease from CNTL = (min-  
689 CNTLp)/CNTLp, where max is largest region-mean LM precipitation value, min is  
690 smallest region-mean LM precipitation value, and CNTLp is region-mean LM  
691 precipitation value in LM CNTL.

		<b>Mogollon sub-region</b>	<b>Salt</b>	<b>Verde</b>
<b>AR Angle</b>	Total percent difference	6%	33%	33%
	Max increase from CNTL	2%	10%	1%
	Max decrease from CNTL	-4%	-18%	-24%
<b>Upstream terrain</b>	Total percent difference	55%	22%	44%
	Max increase from CNTL	14%	6%	7%
	Max decrease from CNTL	-27%	-13%	-26%

692

693

694 **Figure Captions**

695 Fig. 1. Terrain height in the WRF simulations (color fill, km): (a) 81 km resolution, (b) 27 km,  
696 (c) 9 km, (d) 3 km, (e) 3 km BajaTall, and (f) 3 km BajaTaller. Blue boxes in (d) show the four  
697 sub-regions used in Fig. 5, three of which are used in Fig. 2c and one in Figs. 10-13. Red  
698 numbers in (d) mark four locations referred to in the text, with key at bottom left of (d). Black  
699 line shows actual coastline.

700 Fig. 2. 48-hour total precipitation (mm) ending at 1800 UTC 22 Jan. 2010 from (a) Stage IV  
701 QPE and (b) 3km resolution ‘control’ WRF simulation (CNTL), with missing data locations  
702 from (a) removed. White, yellow, and magenta ‘x’ show location of Workman Creek, Marshall  
703 Gulch, and Tucson gauges, respectively. Black line shows actual coastline, dark/medium/light  
704 gray contours show terrain at 500/1500/2500m, and the three blue inset boxes are the same as the  
705 eastern three shown in Fig. 1d. Red numbers in (a) mark four locations referred to in the text,  
706 with key at bottom left of (a). (c) Sub-region mean and maximum 48-hr total precipitation (mm)  
707 ending at 1800 UTC 22 Jan. 2010 from Stage IV QPE and CNTL (see legend for colors).  
708 Missing data locations in Stage IV QPE have been removed from CNTL prior to averaging. (d)  
709 Time series of precipitation accumulation (mm) from Tucson (red), Marshall Gulch (orange),  
710 and Workman Creek (purple) for observations (dashed) and closest CNTL gridpoint (solid).

711 Fig. 3. IVT ( $\text{kg s}^{-1} \text{m}^{-1}$ ) in (a) CFSR and (b) CNTL, on 0000 UTC Jan. 22, 2010. Color contours  
712 and arrows show IVT magnitude and arrows also show direction. Green numbers in (a) mark  
713 four locations referred to in the text, with key at bottom left of Fig. 2a. (c) Time series of hourly  
714 IWV (cm; green) and hourly, layer-mean, along-AR IWV flux ( $\text{cm m s}^{-1}$ ; blue) observed with a  
715 wind profiler and GPS receiver near Tucson, AZ (dashed; from Neiman et al. 2013) and closest

716 CNTL gridpoint (solid). Note that for IWV flux calculation, we have used winds between 900  
717 hPa and 850 hPa (i.e., ~1.0 – 1.5 km MSL), whereas the corresponding observations are between  
718 1.0 and 1.5 km MSL. Cyan and white ‘x’ in top panels show locations of the Tucson 449 MHz  
719 wind profiler and GPS receiver, respectively.

720 Fig. 4. 48-hour total precipitation (mm) ending at 1800 UTC 22 Jan. 2010 in 9 WRF simulations:  
721 (a) 81L81A, (b) 27L27A, (c) 9L9A, (d) 81L3A, (e) 27L3A, (f) 9L3A, (g) CNTL, (h) 3 km  
722 BajaTall, and (i) 3 km BajaTaller. Red numbers in (d) mark four locations referred to in the text,  
723 with key at bottom left of (g). Black line shows actual coastline, and dark/medium/light gray  
724 contours show model terrain at 500/1500/2500m.

725 Fig. 5. Sub-region-wide mean 48-hour total precipitation amount ending at 1800 UTC 22 Jan.  
726 2010 for the nine WRF simulations, normalized by the CNTL areal mean, for (a) Baja, (b)  
727 Mogollon, (c) CO San Juan Mountains, and (d) AZ/MX border. Sub-regions are shown in Fig.  
728 1d. The amount each panel has been normalized by (in mm) is shown at the top of each panel.  
729 Thin red dashed line shows  $y=1$ .

730 Fig. 6. IVT (color fill,  $\text{kg s}^{-1} \text{m}^{-1}$ , integrated from 1000 to 300 hPa) at 0000 UTC Jan 22, 2010 in  
731 9 WRF simulations (as in Fig. 4). The lines AB and CD composed of cyan circles in (g) show  
732 locations of cross sections in Figures 7 and 8, respectively. Green and blue boxes in (g) show  
733 North- and South- Baja regions used in drying ratio calculations in Fig. 9. Green numbers 1 and  
734 2 in (g) show the location of two locations referred to in the text, with key at bottom left of Fig.  
735 2a. Black line shows actual coastline, and dark/medium/light gray contours show terrain at  
736 500/1500/2500m.

737 Fig. 7. Cross section along the spine of Baja (line AB on Fig. 6g) of along-AR VT (color fill, kg  
34

738  $\text{s}^{-1} \text{m}^{-1}$ ) at 0000 UTC Jan 22, 2010 in 9 WRF simulations (as in Fig. 4). The line of cyan circles  
739 AB in Fig. 6g shows the location of this cross section. Grey shading shows model terrain along  
740 this cross section. VT values have been calculated on pressure levels every 50 hPa (e.g., 975 hPa,  
741 925 hPa, etc). Terrain in the coarse-atmosphere simulations (e.g., 81L81A) appears different than  
742 terrain in the fine-atmosphere simulation with the same land resolution (e.g. 81L3A) because a  
743 contouring artifact (i.e., these are not raster-fill images).

744 Fig. 8. Same as Fig. 7, except for the cross section downstream (i.e., east) of Baja (line CD on  
745 Fig. 6g). The black contour in each panel shows maximum upstream elevation.

746 Fig. 9. Drying ratio for entire 48-hour simulation (ending at 1800 UTC 22 Jan. 2010) for the nine  
747 WRF simulations across (a) Northern Baja and (b) Southern Baja, with areas used in calculations  
748 shown in Fig. 6g.

749 Fig. 10. CNTL terrain elevation in Mogollon sub-region (color fill, km), used as terrain for all  
750 LM calculations. Gray-scale contours show terrain at 500, 1500, and 2500m for reference in  
751 Figs. 11 and 12. Magenta lines outline the Verde and Salt River basins of Fig. 14.

752 Fig. 11. 48-hour total precipitation (color fill, mm) ending at 1800 UTC 22 Jan. 2010 in (a)  
753 CNTL and (b) LM using CNTL winds and temperature in the layer between 1000 and 800 hPa  
754 (i.e., LM CNTL). Gray-scale contours show terrain at 500, 1500, and 2500m. Heavy black arrow  
755 in (b) shows mean wind direction (from  $213^\circ$ ) computed in the layer between 1000 and 800 hPa.  
756 Magenta lines outline the Verde and Salt River basins of Fig. 14: West is Verde and east is Salt.

757 Fig. 12. Differences of 48-hour total precipitation (color fill, mm) ending at 1800 UTC 22 Jan.  
758 2010 between LM and LM CNTL (i.e., LM minus LM CNTL), with 1000-800 hPa wind

759 directions shifted by (a) -40, (b) -20, (c) +20, and (d) +40 degrees. Gray-scale contours show  
760 terrain at 500, 1500, and 2500m. Heavy black arrow shows mean wind direction computed in the  
761 layer between 1000 and 800 hPa. Magenta lines outline the Verde and Salt River basins of Fig.  
762 14: West is Verde and east is Salt.

763 Fig. 13. Mogollon region mean normalized 48-hour total precipitation (dimensionless) from LM,  
764 normalized by LM CNTL region mean. Variables necessary to run the LM are taken from (a)  
765 CNTL except shifting winds from from -40 to +40 degrees, by increments of 10 degrees (0 is  
766 CNTL winds which on average is from  $211^\circ$ , computed in the layer between 800 and 1000 hPa),  
767 and (b) the 9 terrain-modification WRF simulations (3km is CNTL). Normalizing factor (i.e.,  
768 LM CNTL precipitation) is 60 mm.

769 Fig. 14. Same as Fig. 13 but for the (a, b) Salt River basin and (c, d) Verde River basin.  
770 Normalizing factors (i.e., LM CNTL precipitation areal means) are (a, b) 127.7 mm (c, d) 104.6  
771 mm.

772 Fig. 15. Conceptual schematic (with color-fill terrain shading, km) of two competing controls on  
773 orographic precipitation amounts investigated in this manuscript. Pink swath shows range of AR  
774 angles where large precipitation amounts are not limited by upstream topography. Blue swath  
775 shows range of AR angles favored by Verde basin local topography for large precipitation  
776 amounts. The overlap of these two swaths shows range of angles for which both favor large  
777 precipitation amounts. Purple arrow shows average angle of winds in AR from CNTL.

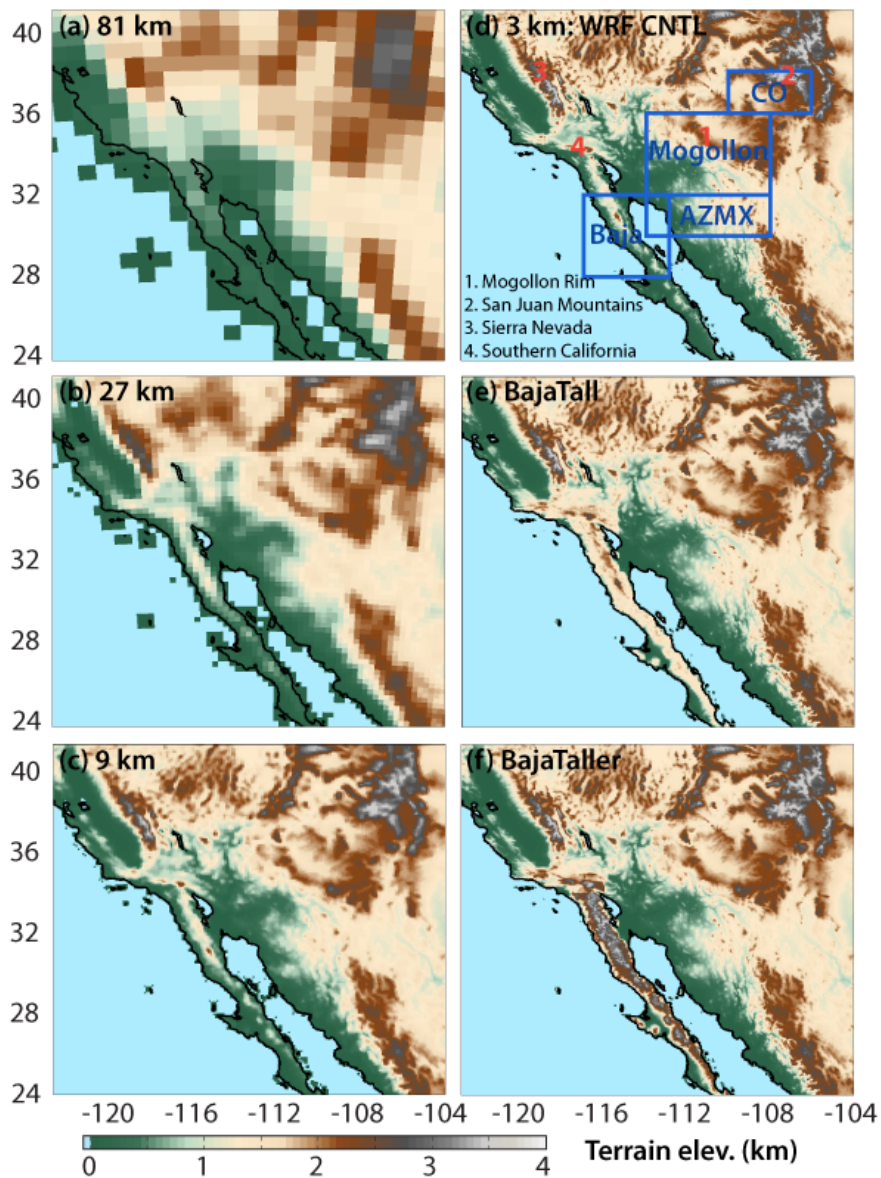


Figure 1: Terrain height in the WRF simulations (color fill, km): (a) 81 km resolution, (b) 27 km, (c) 9 km, (d) 3 km, (e) 3 km BajaTall, and (f) 3 km BajaTaller. Blue boxes in (d) show the four sub-regions used in Fig. 5, three of which are used in Fig. 2c and one in Figs. 10-13. Red numbers in (d) mark four locations referred to in the text, with key at bottom left of (d). Black line shows actual coastline.

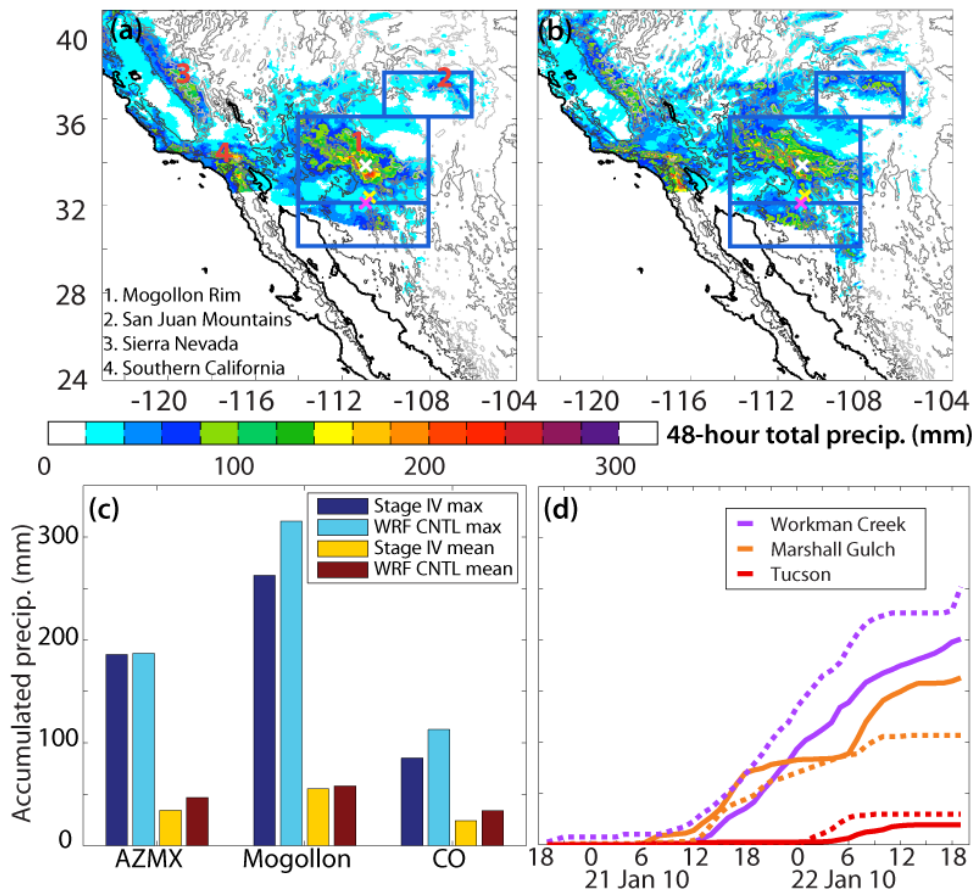


Figure 2: 48-hour total precipitation (mm) ending at 1800 UTC 22 Jan. 2010 from (a) Stage IV QPE and (b) 3km resolution ‘control’ WRF simulation (CNTL), with missing data locations from (a) removed. White, yellow, and magenta ‘x’ show location of Workman Creek, Marshall Gulch, and Tucson gauges, respectively. Black line shows actual coastline, dark/medium/light gray contours show terrain at 500/1500/2500m, and the three blue inset boxes are the same as the eastern three shown in Fig. 1d. Red numbers in (a) mark four locations referred to in the text, with key at bottom left of (a). (c) Sub-region mean and maximum 48-hr total precipitation (mm) ending at 1800 UTC 22 Jan. 2010 from Stage IV QPE and CNTL (see legend for colors). Missing data locations in Stage IV QPE have been removed from CNTL prior to averaging. (d) Time series of precipitation accumulation (mm) from Tucson (red), Marshall Gulch (orange), and Workman Creek (purple) for observations (dashed) and closest CNTL gridpoint (solid).

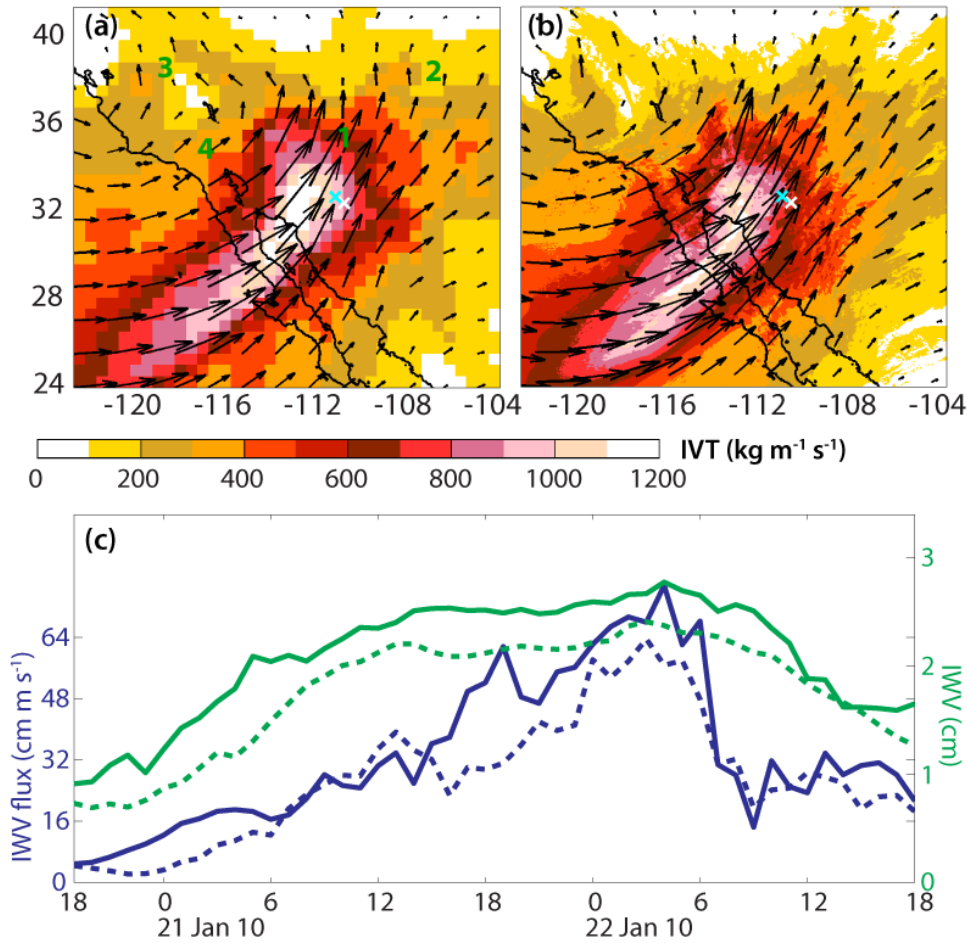


Figure 3: IVT ( $\text{kg s}^{-1} \text{m}^{-1}$ ) in (a) CFSR and (b) CNTL, on 0000 UTC Jan. 22, 2010. Color contours and arrows show IVT magnitude and arrows also show direction. Green numbers in (a) mark four locations referred to in the text, with key at bottom left of Fig. 2a. (c) Time series of hourly IWV (cm; green) and hourly, layer-mean, along-AR IWV flux ( $\text{cm m s}^{-1}$ ; blue) observed with a wind profiler and GPS receiver near Tucson, AZ (dashed; from Neiman et al. 2013) and closest CNTL gridpoint (solid). Note that for IWV flux calculation, we have used winds between 900 hPa and 850 hPa (i.e.,  $\sim 1.0 - 1.5$  km MSL), whereas the corresponding observations are between 1.0 and 1.5 km MSL. Cyan and white 'x' in top panels show locations of the Tucson 449 MHz wind profiler and GPS receiver, respectively.



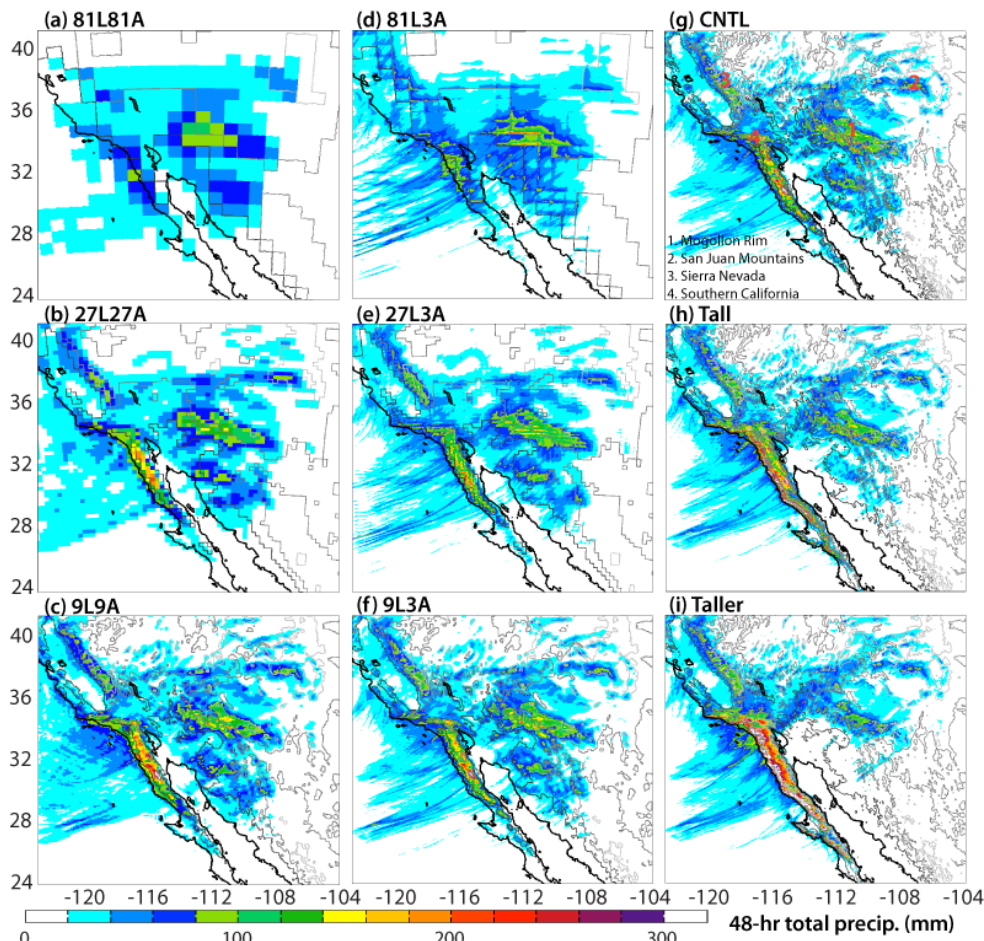


Figure 4: 48-hour total precipitation (mm) ending at 1800 UTC 22 Jan. 2010 in 9 WRF simulations: (a) 81L81A, (b) 27L27A, (c) 9L9A, (d) 81L3A, (e) 27L3A, (f) 9L3A, (g) CNTL, (h) 3 km BajaTall, and (i) 3 km BajaTaller. Red numbers in (d) mark four locations referred to in the text, with key at bottom left of (g). Black line shows actual coastline, and dark/medium/light gray contours show model terrain at 500/1500/2500m.

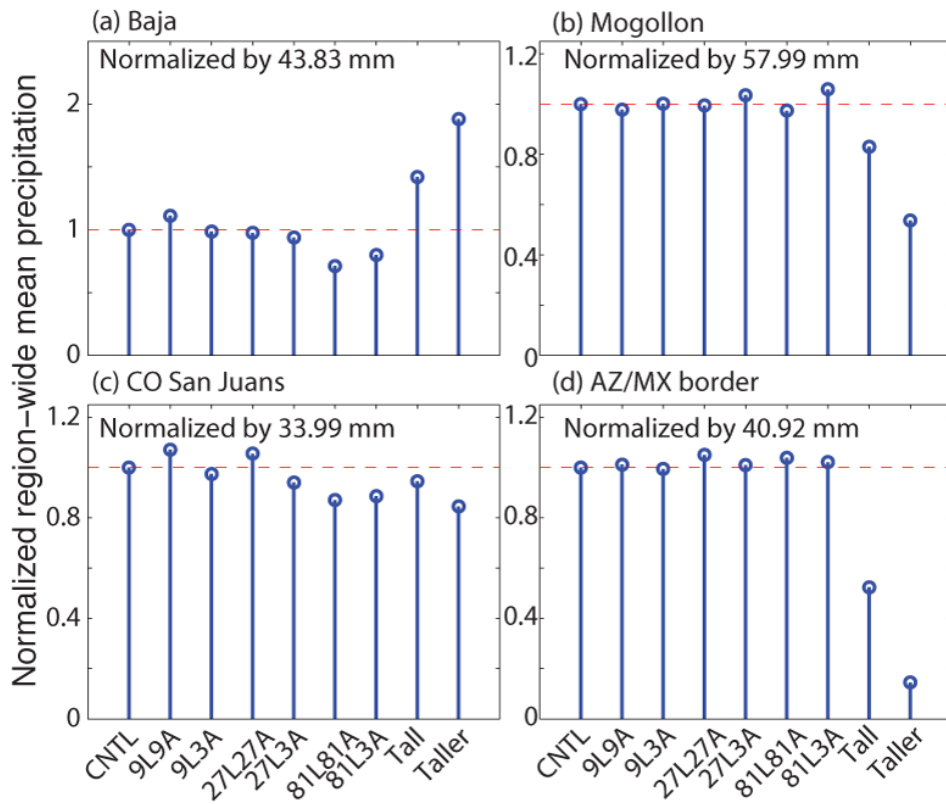


Figure 5: Sub-region-wide mean 48-hour total precipitation amount ending at 1800 UTC 22 Jan. 2010 for the nine WRF simulations, normalized by the CNTL areal mean, for (a) Baja, (b) Mogollon, (c) CO San Juan Mountains, and (d) AZ/MX border. Sub-regions are shown in Fig. 1d. The amount each panel has been normalized by (in mm) is shown at the top of each panel. Thin red dashed line shows  $y=1$ .

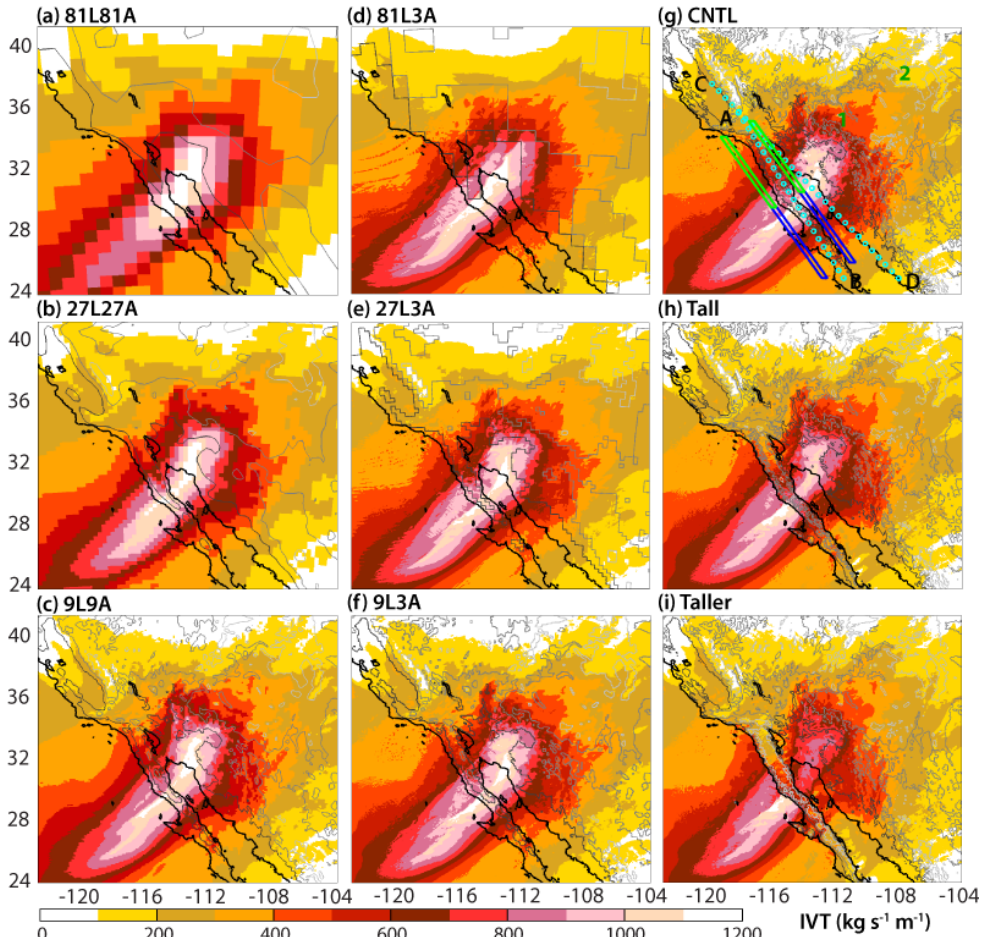


Figure 6: IVT (color fill,  $\text{kg s}^{-1} \text{m}^{-1}$ , integrated from 1000 to 300 hPa) at 0000 UTC Jan 22, 2010 in 9 WRF simulations (as in Fig. 4). The lines AB and CD composed of cyan circles in (g) show locations of cross sections in Figures 7 and 8, respectively. Green and blue boxes in (g) show North- and South- Baja regions used in drying ratio calculations in Fig. 9. Green numbers 1 and 2 in (g) show the location of two locations referred to in the text, with key at bottom left of Fig. 2a. Black line shows actual coastline, and dark/medium/light gray contours show terrain at 500/1500/2500m.

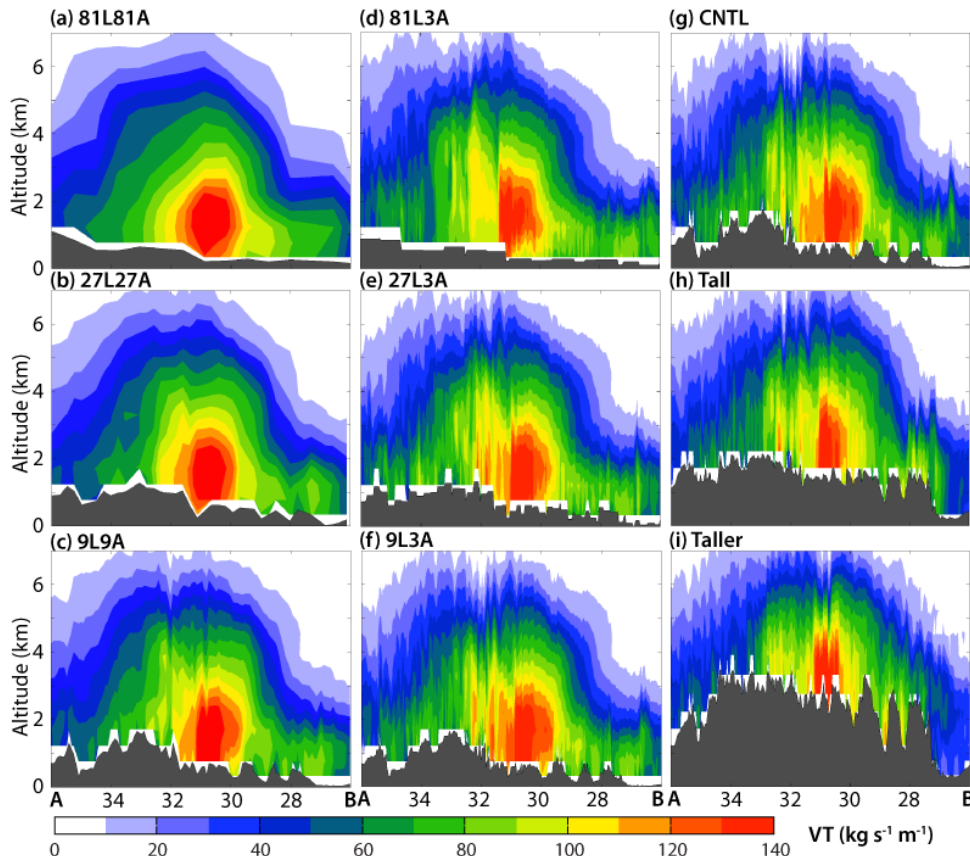


Figure 7: Cross section along the spine of Baja (line AB on Fig. 6g) of along-AR VT (color fill,  $\text{kg s}^{-1} \text{m}^{-1}$ ) at 0000 UTC Jan 22, 2010 in 9 WRF simulations (as in Fig. 4). The line of cyan circles AB in Fig. 6g shows the location of this cross section. Grey shading shows model terrain along this cross section. VT values have been calculated on pressure levels every 50 hPa (e.g., 975 hPa, 925 hPa, etc). Terrain in the coarse-atmosphere simulations (e.g., 81L81A) appears different than terrain in the fine-atmosphere simulation with the same land resolution (e.g. 81L3A) because a contouring artifact (i.e., these are not raster-fill images).

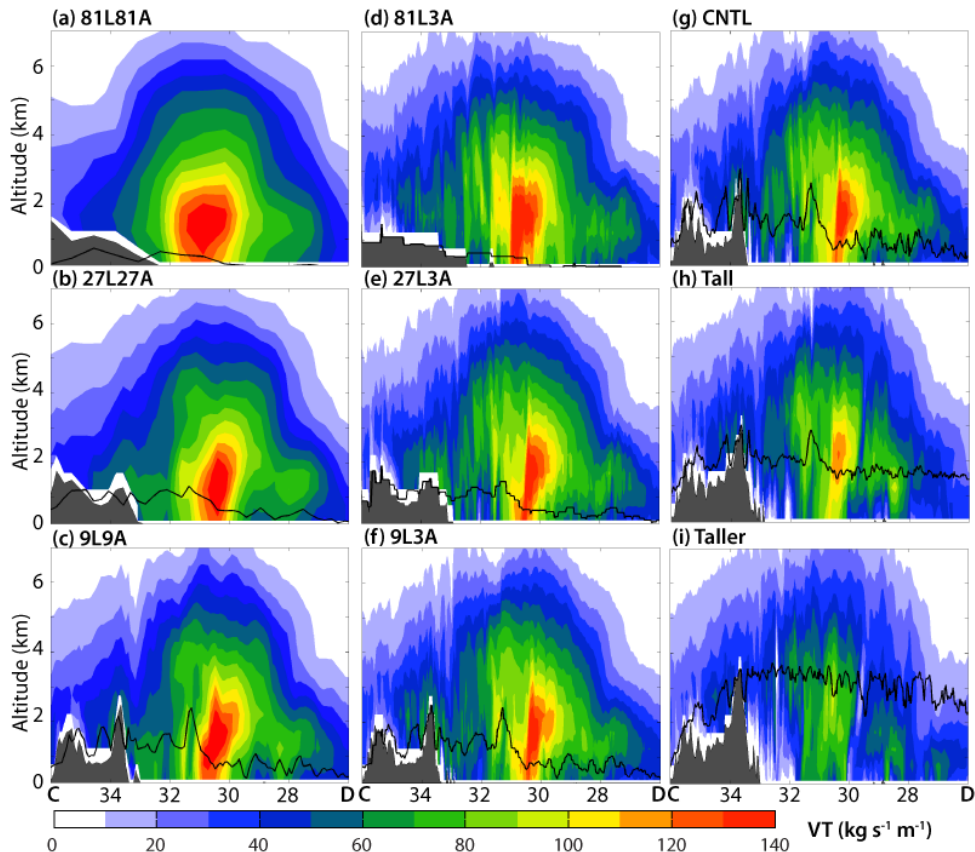
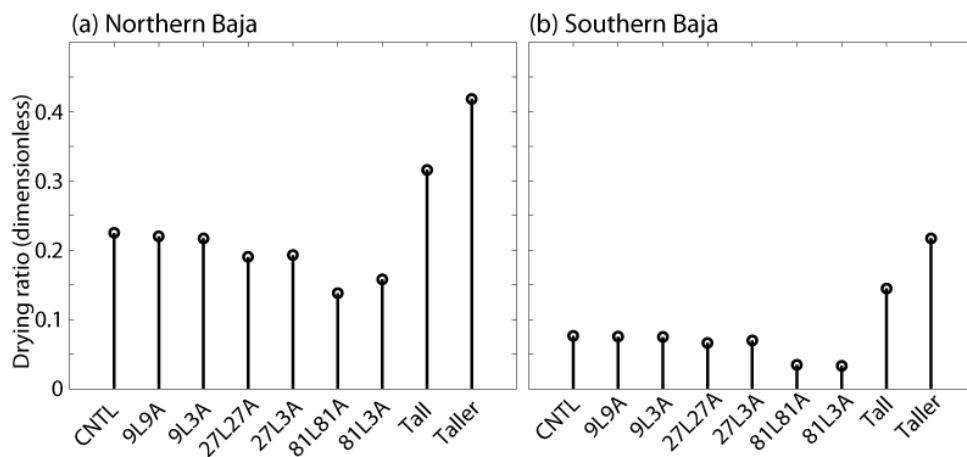


Figure 8: Same as Fig. 7, except for the cross section downstream (i.e., east) of Baja (line CD on Fig. 6g). The black contour in each panel shows maximum upstream elevation.

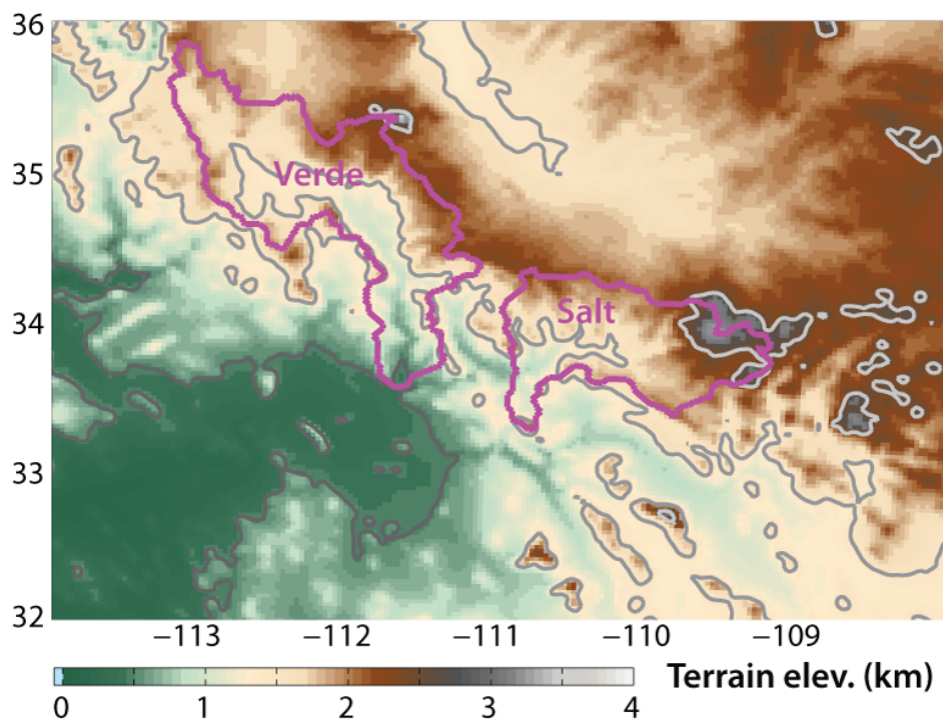


842

843 Figure 9: Drying ratio for entire 48-hour simulation (ending at 1800 UTC 22 Jan. 2010) for the  
 844 nine WRF simulations across (a) Northern Baja and (b) Southern Baja, with areas used in  
 845 calculations shown in Fig. 6g.

846





847

848 Figure 10: CNTL terrain elevation in Mogollon sub-region (color fill, km), used as terrain for all  
 849 LM calculations. Gray-scale contours show terrain at 500, 1500, and 2500m for reference in  
 850 Figs. 11 and 12. Magenta lines outline the Verde and Salt River basins of Fig. 14.

851

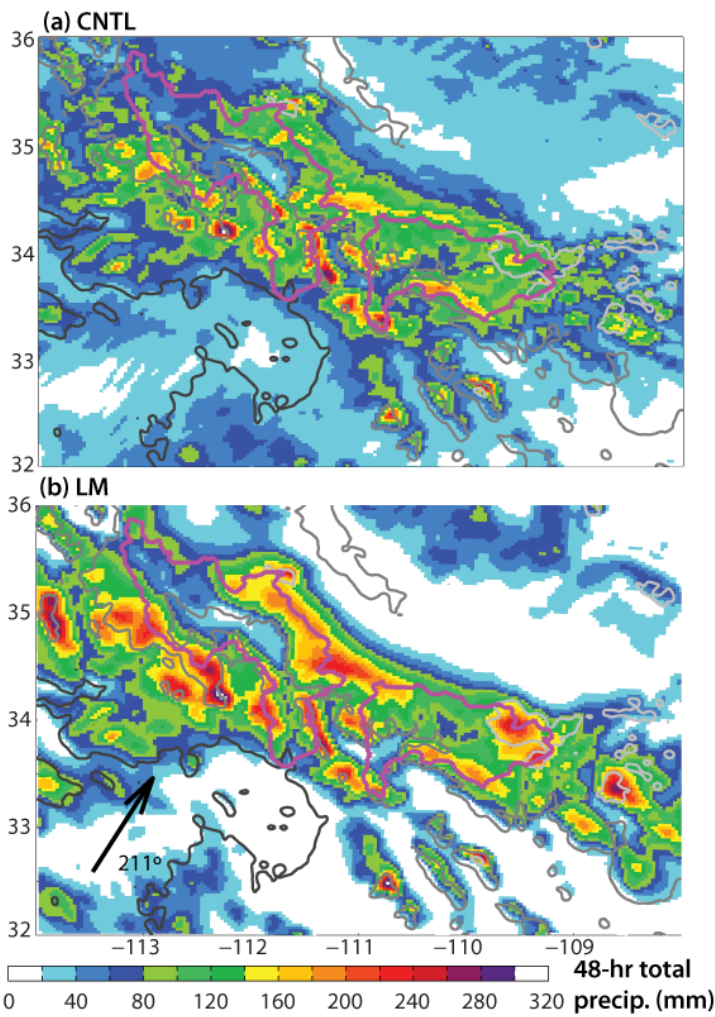


Figure 11: 48-hour total precipitation (color fill, mm) ending at 1800 UTC 22 Jan. 2010 in (a) CNTL and (b) LM using CNTL winds and temperature in the layer between 1000 and 800 hPa (i.e., LM CNTL). Gray-scale contours show terrain at 500, 1500, and 2500m. Heavy black arrow in (b) shows mean wind direction (from 213°) computed in the layer between 1000 and 800 hPa. Magenta lines outline the Verde and Salt River basins of Fig. 14: West is Verde and east is Salt.



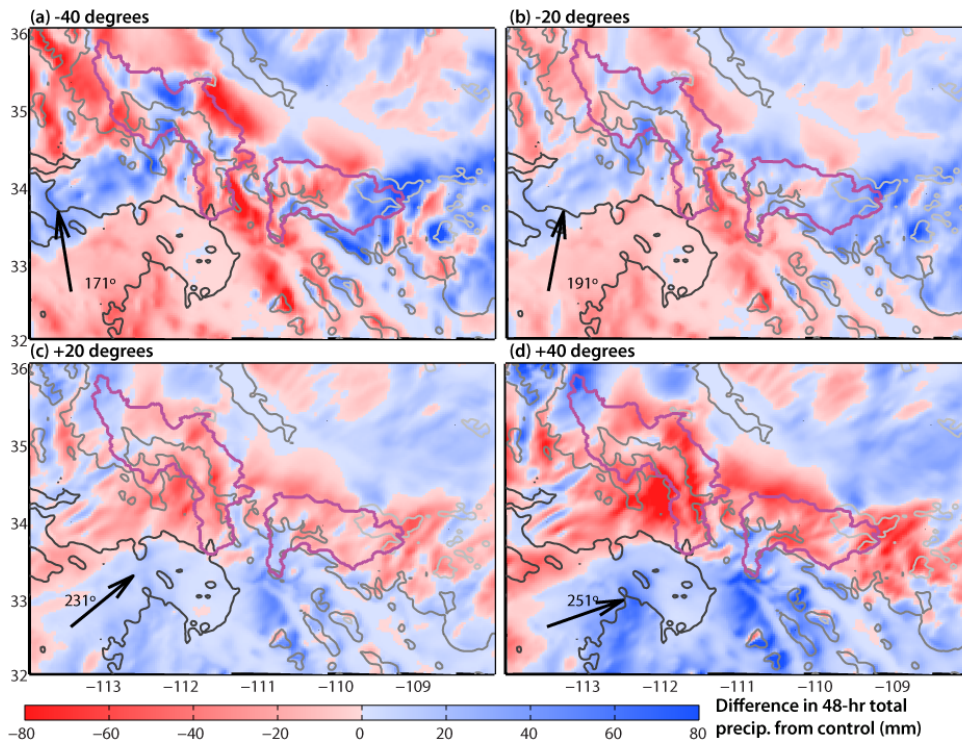


Figure 12: Differences of 48-hour total precipitation (color fill, mm) ending at 1800 UTC 22 Jan. 2010 between LM and LM CNTL (i.e., LM minus LM CNTL), with 1000-800 hPa wind directions shifted by (a) -40, (b) -20, (c) +20, and (d) +40 degrees. Gray-scale contours show terrain at 500, 1500, and 2500m. Heavy black arrow shows mean wind direction computed in the layer between 1000 and 800 hPa. Magenta lines outline the Verde and Salt River basins of Fig. 14: West is Verde and east is Salt.

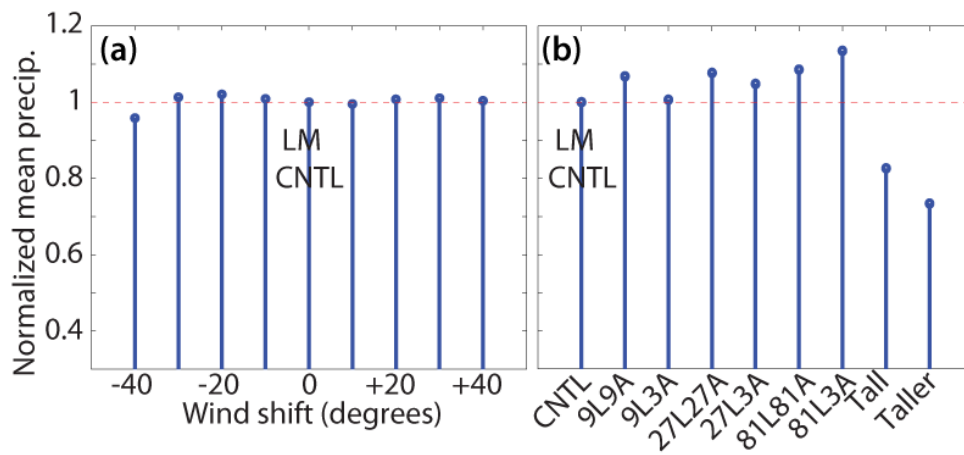


Figure 13: Mogollon region mean normalized 48-hour total precipitation (dimensionless) from LM, normalized by LM CNTL region mean. Variables necessary to run the LM are taken from (a) CNTL except shifting winds from from -40 to +40 degrees, by increments of 10 degrees (0 is CNTL winds which on average is from 211°, computed in the layer between 800 and 1000 hPa), and (b) the 9 terrain-modification WRF simulations (3km is CNTL). Normalizing factor (i.e., LM CNTL precipitation) is 60 mm.

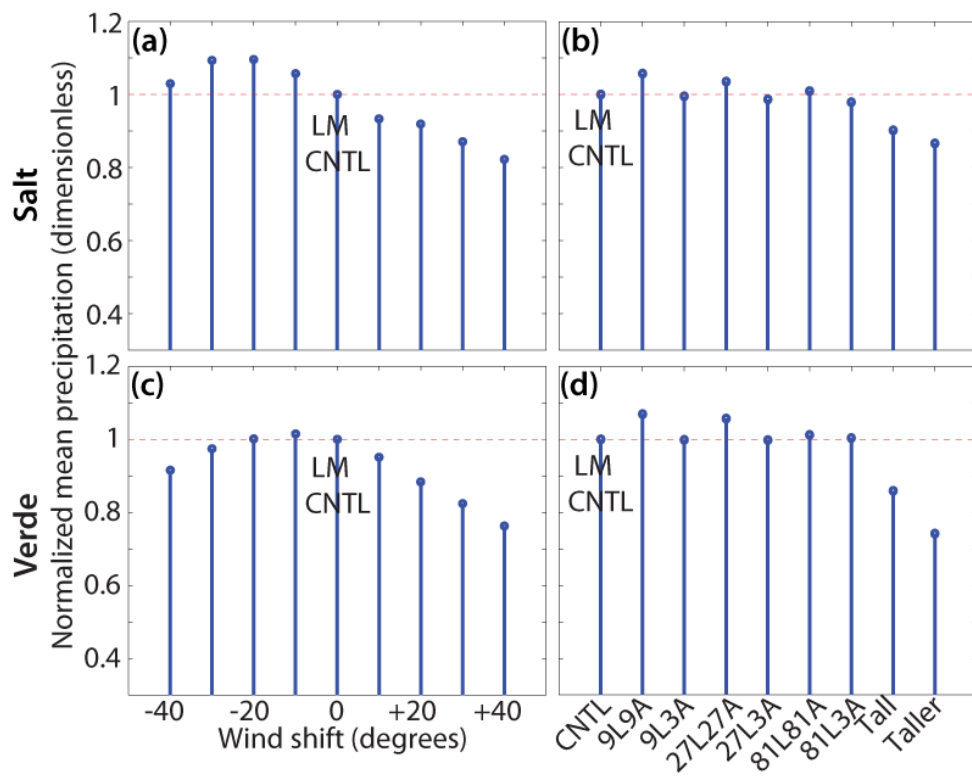
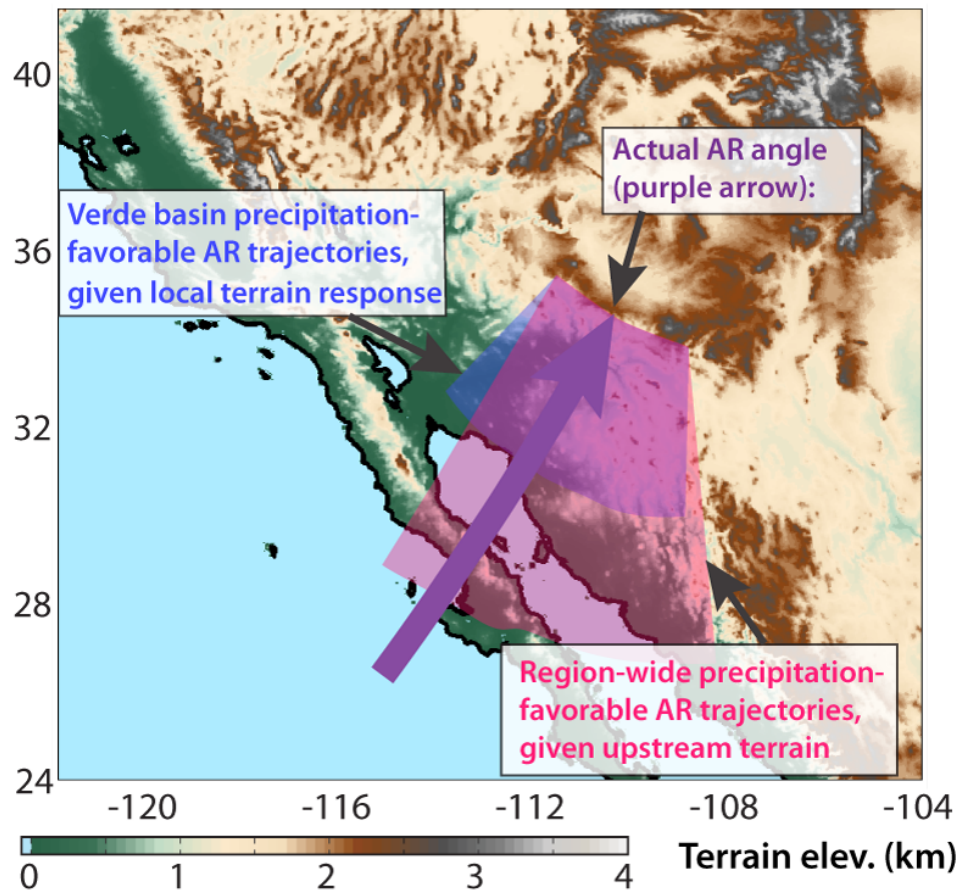


Figure 14: Same as Fig. 13 but for the (a, b) Salt River basin and (c, d) Verde River basin. Normalizing factors (i.e., LM CNTL precipitation areal means) are (a, b) 127.7 mm (c, d) 104.6 mm.



881  
 882 Figure 15: Conceptual schematic (with color-fill terrain shading, km) of two competing controls  
 883 on orographic precipitation amounts investigated in this manuscript. Pink swath shows range of  
 884 AR angles where large precipitation amounts are not limited by upstream topography. Blue  
 885 swath shows range of AR angles favored by Verde basin local topography for large precipitation  
 886 amounts. The overlap of these two swaths shows range of angles for which both favor large  
 887 precipitation amounts. Purple arrow shows average angle of winds in AR from CNTL.  
 888